IOE | Intelligent Opto-Electronics

Research progress in integrated optics for optical coherence tomography

Qianqian Song, Dawei Zhang, Zhihua Ding, Guoqiang Li*

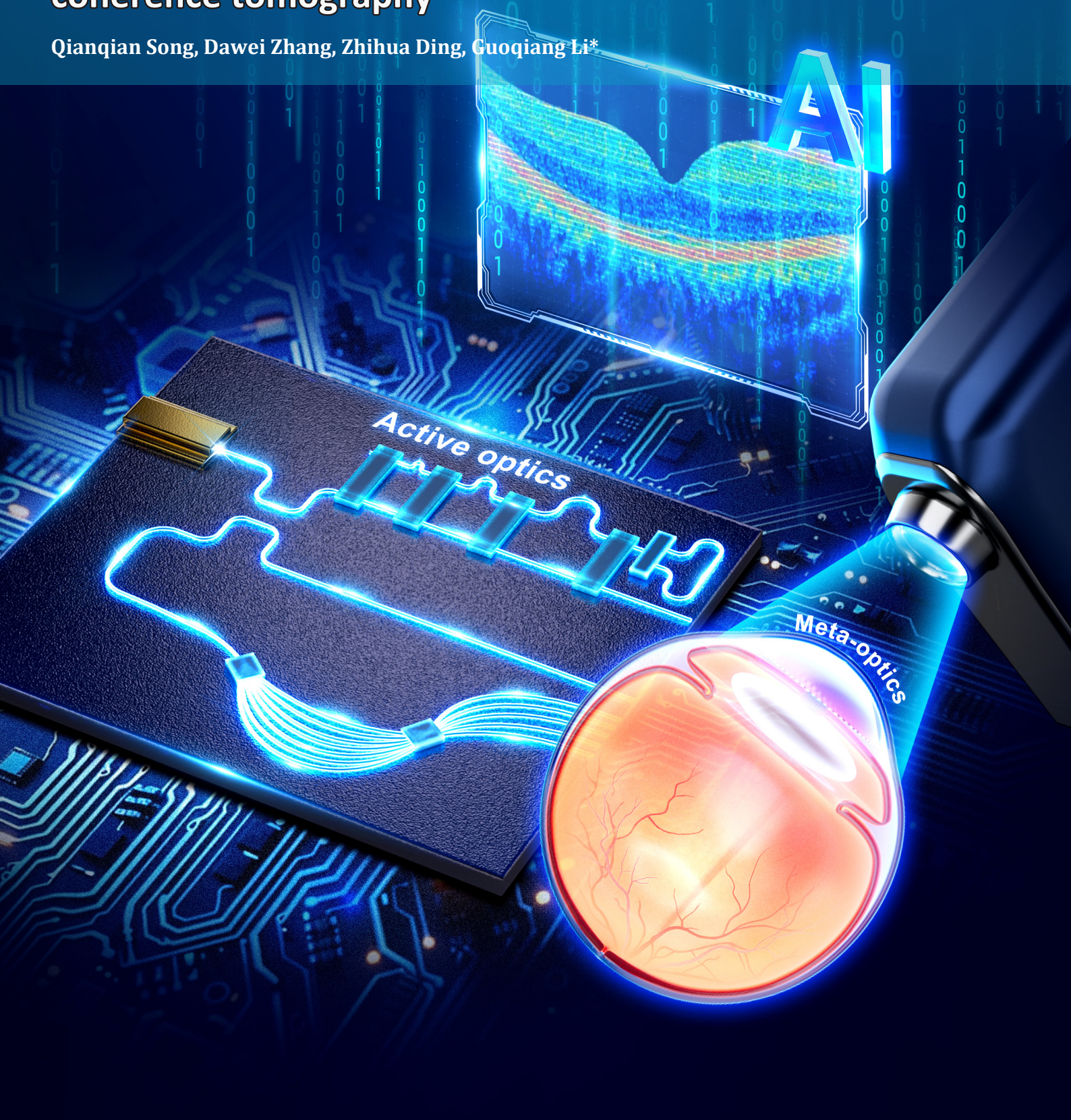

IOE | Intelligent Opto-Electronics

Research progress in integrated optics for optical coherence tomography

Qianqian Song, Dawei Zhang, Zhihua Ding and Guoqiang Li

Citation: Song QQ, Zhang DW, Ding ZH, et al. Research progress in integrated optics for optical coherence tomography. *Intelligent Opto-Electronics* **2**, 250009 (2026).

https://doi.org/10.29026/ioe.2026.250009

Received: 14 September 2025; Accepted: 18 November 2025; Published online: 25 March 2026

IOE | Intelligent Opto-Electronics

Review

March 2026, Vol. 2, No. 1

Open Access

Research progress in integrated optics for optical coherence tomography

Qianqian Song[1,2,3], Dawei Zhang[4], Zhihua Ding[5,6] and Guoqiang Li[1]*

Abstract: Optical coherence tomography (OCT) is a noninvasive biomedical imaging technique that exploits the back-reflection and scattering properties of tissue without the need for exogenous contrast agents. It enables high-resolution, in situ visualization of tissue microstructures and pathological features, without requiring specimen removal or processing. OCT offers cross-sectional and three-dimensional imaging of biological tissues with micron-level resolution and millimeter-scale depths. When integrated with an endoscope, OCT becomes a powerful and versatile imaging tool in the medical field. However, conventional OCT systems face several limitations, including a bulky system volume of approximately 1 m^3, high costs of around $100,000, operational complexity, limited portability, and the need for precise optical alignment, which demands substantial manpower and time. To overcome these challenges, integrated optics has emerged as a promising solution. In recent years, significant advances have been made in developing OCT systems based on integrated photonics. All the integrated-optics devices, such as light sources, isolators, couplers, circulators, detectors, and active optical components, can be exploited for endoscopic and non-endoscopic OCT systems and enable more compact designs and implementations. This review provides a comprehensive overview of these advancements. We first summarize the fundamental principles and imaging properties of OCT, along with the design and functionality of OCT endoscopic probes. We then examine the recent progress in on-chip OCT systems, focusing on system optimization and the implementation of integrated photonic technologies. Finally, we discuss the current challenges, including the full integration of optical components onto a single chip, and explore prospects of integrated-optics based OCT endoscopy, particularly the integration of AI-powered intelligent diagnostics to enhance real-time clinical decision-making and expand the applications of OCT in personalized medicine.

Keywords: optical coherence tomography; imaging; endoscope; integrated optics

DOI: 10.29026/ioe.2026.250009

Citation: Song QQ, Zhang DW, Ding ZH et al. Research progress in integrated optics for optical coherence tomography. *Intell Opto-Electron* **2**, 250009 (2026).

1 Introduction

With the rapid advancements of medical and imaging technologies, non-invasive and minimally invasive diagnostic and therapeutic methods have become increasingly preferred. This trend has driven the development of numerous endoscopic imaging technologies, significantly enhancing image resolution and contrast.

Since its introduction by Huang et al. in 1991[1], optical coherence tomography (OCT) has demonstrated immense potential across various medical fields, owing to its high resolution and non-invasive nature. OCT has become particularly valuable in clinical applications such as ophthalmology[2], gastroenterology[3,4], cardiology[5], pulmonology[6], gynecology[7,8], and urology[9], with an especially indispensable

Received: 14 September 2025

Accepted: 18 November 2025

Published online: 25 March 2026

[1]Intelligent Optical Imaging and Sensing Group, Institute of Optoelectronics, College of Future Information Technologies, State Key Laboratory of Photovoltaic Science and Technology, Shanghai Frontier Base of Intelligent Optoelectronics and Perception, Fudan University, Shanghai 200438, China; [2]Westlake Institute for Optoelectronics, Westlake University, Hangzhou 311400,China; [3]Research Center for Frontier Fundamental Studies, Zhejiang Lab, Hangzhou 311100, China; [4]Ministry of Education and Shanghai Key Lab of Modern Optical System, Shanghai Environmental Biosafety Instruments and Equipment Engineering Technology Research Center, University of Shanghai for Science and Technology, Shanghai 200093, China; [5]ZJU-Hangzhou Global Scientific and Technological Innovation Center, Zhejiang University, Hangzhou 311215, China; [6]State Key Laboratory of Extreme Photonics and Instrumentation, College of Optical Science and Engineering, Zhejiang University, Hangzhou 310027, China.
*Correspondence: GQ Li, E-mail: gqli2001@gmail.com; gqli@fudan.edu.cn

in optometry and ophthalmology.

In these fields, OCT endoscopy plays a pivotal role in visualizing internal lesions within the human body. Its ability to provide high imaging quality combined with operational convenience is essential for early disease diagnosis, accurate analysis, treatment planning, and pre- and post-treatment assessments. While traditional endoscopic techniques such as white light endoscopy (WLE) excel at capturing the external morphology of lesions, they often fail to resolve microscopic and deep-tissue structures. OCT endoscopy overcomes these shortcomings by offering superior resolution and depth, thereby enhancing diagnostic accuracy and providing more detailed information for clinical decision-making.

OCT endoscopy utilizes tissue reflection and scattering properties to enable cross-sectional tomographic imaging and three-dimensional (3D) visualization of biological structures at micron-level resolution and millimeter-scale depths—without the need for exogenous contrast agents[10,11]. Additionally, OCT enables real-time "optical biopsy"[12,13], offering direct visualization of tissue microstructures and pathological changes in situ. This approach eliminates the need for specimen processing or removal, which is a significant advantage over traditional biopsy techniques[12–15]. Beyond providing detailed visual representation, OCT endoscopy offers invaluable insights into the internal structures of lesions. This capability equips physicians with a comprehensive diagnostic tool that not only helps in identifying lesions but also enhances the understanding of tissue composition and pathology. Moreover, the miniaturized design of OCT endoscopic probes facilitates access to narrow lumens and blood vessels, thus expanding the range of clinical applications.

In the field of photodynamic therapy (PDT), OCT enables real-time, non-invasive monitoring of photosensitizer distribution within target tissues. It also allows observation of lesion morphology before, during, and after laser irradiation, providing critical feedback for assessing therapeutic efficacy and guiding treatment decisions.

Despite its numerous advantages, several limitations persist in current OCT endoscopy systems. These include their large volume (~1 m^3)[16], high cost (~$100,000)[16,17], operational complexity, and stringent alignment requirements, which hinder their widespread adoption in biomedical and optical applications. A promising solution to these challenges lies in the integration of optics technologies, which can make OCT endoscopy systems more compact, mechanically robust, precisely aligned, cost-efficient, mass-producible, and temperature-stable. Significant efforts are being made to address these limitations and realize these goals.

This paper reviews recent research progress in integrated optics for OCT, with a particular focus on how advances in photonic integration has addressed the limitations of traditional OCT systems. It also explores potential imaging applications of integrated optics within OCT-related systems. By enabling significant miniaturization, integrated optics paves the way for more compact designs in both endoscopic and non-endoscopic OCT systems. Both conventional OCT (non-endoscopic OCT) and endoscopic OCT systems can benefit from integrated optics, making their system more compact and efficient. We begin by outlining the systems and fundamental principles of OCT endoscopy, including its imaging system, principles, performance characteristics, probe designs, and recent technological advances. We then introduce the concept of photonic integration on a chip and summarize its relevance to OCT. Building on this, we explore the latest developments in integrated-optics OCT systems, emphasizing key technological innovations, system optimizations, and applications. In addition, we discuss the integration of OCT with other imaging modalities and explore the potential of integrated optics in multimodal systems. Finally, we analyze the current challenges facing integrated-optics-based OCT and offer perspectives on future research directions, including the full integration of optical components onto a single chip, integrated optics-based OCT endoscopy, and particularly the integration of AI-powered intelligent diagnostics to enhance real-time clinical decision-making and expand the applications of OCT in personalized medicine. The overall structure of this review is illustrated in Fig. 1.

2 Fundamentals of OCT endoscopy

2.1 OCT endoscopy system and principle

OCT is an imaging modality based on a low-coherence Michelson interferometer[1]. In an OCT endoscope, a miniature

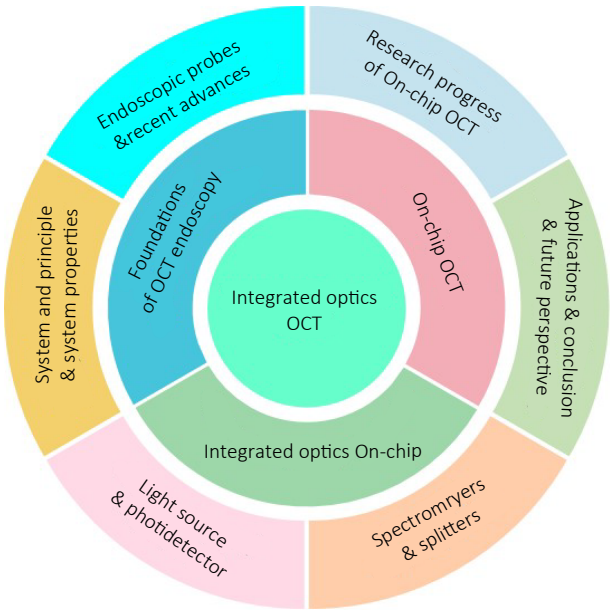

Fig. 1 | Schematic showing the overall outline of this review, including foundations of OCT endoscopy, integrated optics on-chip, and on-chip OCT.

probe (typically inserted into cavity organs or blood vessels) delivers and collects light within the tissue. By precisely measuring the time delay and intensity of light reflected from vessel walls or tissue structures, the system converts positional information into digital signals. These signals are then processed and reconstructed into 2D and 3D images, providing high-resolution, in situ visualization of tissue microstructures.

Over the past few decades, OCT technology has undergone significant improvements in imaging resolution, detection sensitivity, signal-to-noise ratio (SNR), and data acquisition speed. Fourier Domain OCT (FD-OCT), first proposed for medical applications by Fercher et al. in 1995[18], has become the predominant approach due to its higher speed and superior SNR, effectively supplanting time-domain OCT (TD-OCT). Unlike TD-OCT, which requires mechanical scanning of a reference mirror to measure the echo time delays of reflected light, FD-OCT acquires depth information directly via spectral interferometry. This is achieved by using either a broadband light source with a spectrometer (linear detector array) or a rapidly tunable laser source with a single detector. A schematic diagram of a typical FD-OCT system is shown in Fig. 2[19-21].

In FD-OCT, the optical beam delivered to the sample arm is focused on the tissue, and the echo time delay of reflections from different depths is measured by analyzing the spectrum. Interference fringes are produced when light from the reference and sample arms has nearly identical optical path lengths (within the coherence length of the source). By employing a Michelson interferometer with a broadband or swept-source light, FD-OCT can achieve high-resolution imaging of biological tissue comparable to excisional biopsy and histopathology—without the need for tissue removal or contrast agents[22–24]. Operation at near-infrared (NIR) wavelengths further enables deeper tissue penetration (up to ~ 3 mm), expanding the clinical utility of FD-OCT.

In a typical FD-OCT endoscopy system (Fig. 2), detection is accomplished with a spectrometer and a one-dimensional (1D) detector array. This configuration eliminates the need for a moving reference mirror or tunable delay line in the reference arm. Backscattered light from the sample interferes with the reference beam, and the combined interference signal is spectrally dispersed by a diffraction grating such that different wavelengths are focused onto distinct pixels of the 1D detector. By capturing this spectrum and applying a Fourier transform, depth-resolved information is obtained without mechanical depth scanning. Both spectral-domain (SD) OCT and swept-source (SS) OCT implementations of FD-OCT exploit this principle to achieve imaging speeds that are orders of magnitude faster than traditional TD-OCT approaches.

The concepts of SD-OCT and SS-OCT were first introduced by Fercher in 1996[25]. Since then, numerous implementations of FD-OCT systems have been demonstrated. Early examples include an SS-OCT system by Chinn and

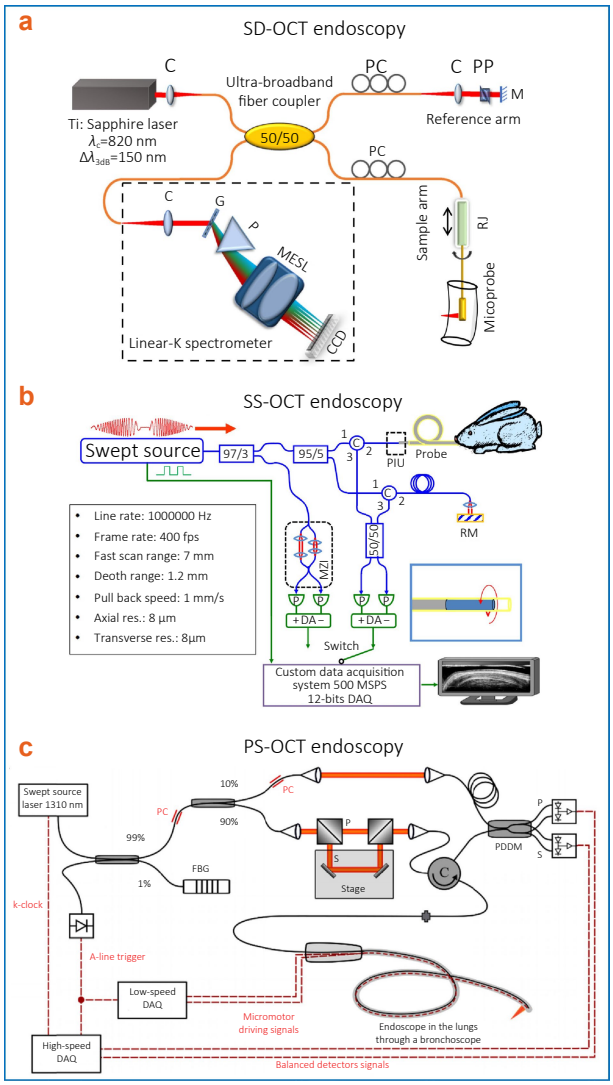

Fig. 2 | Schematic diagram of FD-OCT system. (a) SD-OCT endoscopy Peproduced under the terms of a CC-BY license.[19]Copyright 2017, The Authors. Published by Springer Nature. C: achromatic collimator, CCD: line scan charge-coupled device, G: grating, M: mirror, MESL: multi-element scan lens, P: linear-K mapping prism, PC: polarization controller, PP: prism pair; RJ: fiber-optic rotary joint. (b) SS-OCT endoscopy, Reproduced with permission.[20]Copyright 2013, The Optical Society. C: circulator, MZI: Mach-Zehnder interferometer, RM: reference mirror, DA: differential amplifier; P: photodetector; PIU: patient interface unit. (c) PS-OCT endoscopy, FBG: fiber Bragg grating, C: circulator, PDDM: polarization diversity detection module. Reproduced with permission.[21]Copyright 2019, The Optical Society.

Fujimoto[26] and SD-OCT by Mojrkowski and Fercher[27]. Additionally, a full-field SS-OCT approach employing a wavelength-tunable laser and a diffractive lens has been reported[28]. Since around 2000, research efforts have largely focused on advancing FD-OCT technology, resulting in major developments in both SD-OCT[19] and SS-OCT[20] (as illustrated in Fig. 2(a,b), respectively). These FD-OCT techniques extract depth information by performing a Fourier transform on the detected spectral data, thus enabling rapid

imaging and comprehensive tissue diagnostics. Such improvements have provided a stronger foundation for clinical evaluation and disease diagnosis[18,26,29].

However, in many biological tissue assessments — particularly for early-stage disease detection—the structural differences between healthy and pathological tissues are often extremely subtle. Consequently, conventional structural OCT imaging alone may provide insufficient intrinsic contrast to distinguish normal from diseased states reliably. This limitation underscores the need for enhanced OCT imaging techniques that offer additional contrast mechanisms.

Conventional OCT relies on the intensity of backscattered light to form images. In contrast, functional OCT technologies exploit additional properties of the backscattered light to extract more information about tissue. Notable examples include, Doppler OCT leverages the optical Doppler effect to measure blood flow by detecting frequency shifts in moving scatterers (e.g. blood cells), polarization-sensitive OCT (PS-OCT) uses polarized light and analyzes polarization changes caused by tissue birefringence, revealing microstructural and composition differences (as shown in Fig. 2(c)[21]), OCT angiography (OCTA) computes motion contrast from consecutive OCT scans to reconstruct three-dimensional blood vessel networks without dyes. These functional imaging techniques provide detailed insights into tissue structure, spectral characteristics of biological tissue, polarization effects, blood vessel architecture, and blood flow velocity. Importantly, they offer enhanced tissue characterization in early disease stages, where purely structural imaging may lack the contrast to distinguish healthy versus pathological tissue.

2.2 OCT endoscopy system properties

The performance of an OCT endoscopy system is determined by several key properties. Important parameters include axial resolution (Δz), lateral resolution (Δx), imaging depth, sensitivity or dynamic range, and imaging speed[30]. Fourier-domain OCT (FD-OCT) (which includes SD-OCT and SS-OCT) has largely supplanted TD-OCT in endoscopic applications because it acquires depth-resolved information in the spectral domain and uses Fourier transforms to reconstruct the image. This affords much faster imaging speeds and higher signal-to-noise ratios, enabling real-time imaging at high resolution.

The axial resolution (Δz) defines the ability to resolve fine details along the depth (longitudinal) direction. It is primarily determined by the light source's center wavelength (λ_0) and bandwidth ($\Delta\lambda$). In an ideal case (assuming a Gaussian spectrum), the axial resolution can be expressed as

$$\Delta z = \frac{2\ln 2}{\pi}\frac{\lambda_0^2}{n_s \Delta\lambda}, \tag{1}$$

where n_s is the refractive index of the sample, from this relationship, a broader optical bandwidth $\Delta\lambda$ yields a smaller Δz (better axial resolution), while a longer center wavelength λ_0 yields a larger Δz (poorer resolution). In other words, axial resolution improves (numerically decreases) with increasing source bandwidth, and worsens (increases) with longer central wavelengths. Δz as a function of $\Delta\lambda$ and λ_0 is shown in Fig. 3(a,b), respectively. In Fig. 3(a), Δz is plotted as a function of optical bandwidth $\Delta\lambda$, assuming a fixed central wavelength (λ_0) and a refractive index of n_s = 1.38. Δz decreases as the optical bandwidth $\Delta\lambda$ increases, and Δz increases as λ_0 increases. Notably, Δz is independent of the number of sampling points N_s used in the spectral measurement (Fig. 3(b) confirms that curves for different N_s overlap for the resolution Δz). However, dispersion, absorption, and scattering properties in tissue can also limit the effective axial resolution.

The maximum imaging depth of an FD-OCT system is influenced by the central wavelength of the swept or broadband source, the optical power, and the spectrometer or detector resolution. The OCT system detects the intensity of the interference signal in the wave number domain. As the imaging depth increases, the interference fringes in the spectral data occur at a higher frequency. According to the Nyquist sampling theorem, the photodetector's spectral sampling interval (or the camera's pixel size in SD-OCT, or tuning step in SS-OCT) limits the depth range. Since photodetector sampling is discrete (with time being discrete in SS-OCT and space being discrete in SD-OCT), the sampling rate has an upper limit. The sampling frequency must be at least twice the frequency of the band-limited signal to retain and recover the information in the original signal accurately. Therefore, the bandwidth of the system detector should accommodate the highest frequency $2k\,(\mathrm{t})\,z_{\max}$ of the interference spectral signal at the maximum imaging depth $z_{\max}$. Assuming ideal sampling and no dispersion, the maximum imaging depth $z_{\max}$ can be expressed as

$$z_{\max} = \frac{\lambda_0^2}{4n_s\delta\lambda}, \tag{2}$$

where $\delta\lambda = \Delta\lambda / N_s$ is the sampling spectrum interval, or the wavelength resolution of the spectrometer, $\Delta\lambda$ represents the spectral tuning range of the swept source, and N_s is the number of samples taken by the imaging system during one scanning period, or the number of CCD pixel points. A high number of camera pixels (or sampling points Ns) and a longer wavelength allow a deeper imaging range, while a broader source bandwidth (larger $\Delta\lambda$, hence larger $\delta\lambda$ for a fixed N_s) will reduce the maximum depth. This is illustrated in Fig. 3(b) with a fixed optical bandwidth and n_s = 1.38, for various numbers of sampling points, such as N_s = 1024 (solid lines), N_s = 2048 (dashed lines), and N_s = 512 (dotted lines), where for a given N_s the imaging depth increases with λ_0, and for a given λ_0 the depth increases with more sampling points N_s (e.g., 2048 vs 1024), but decreases if the optical bandwidth is enlarged. Besides, optical attenuation in

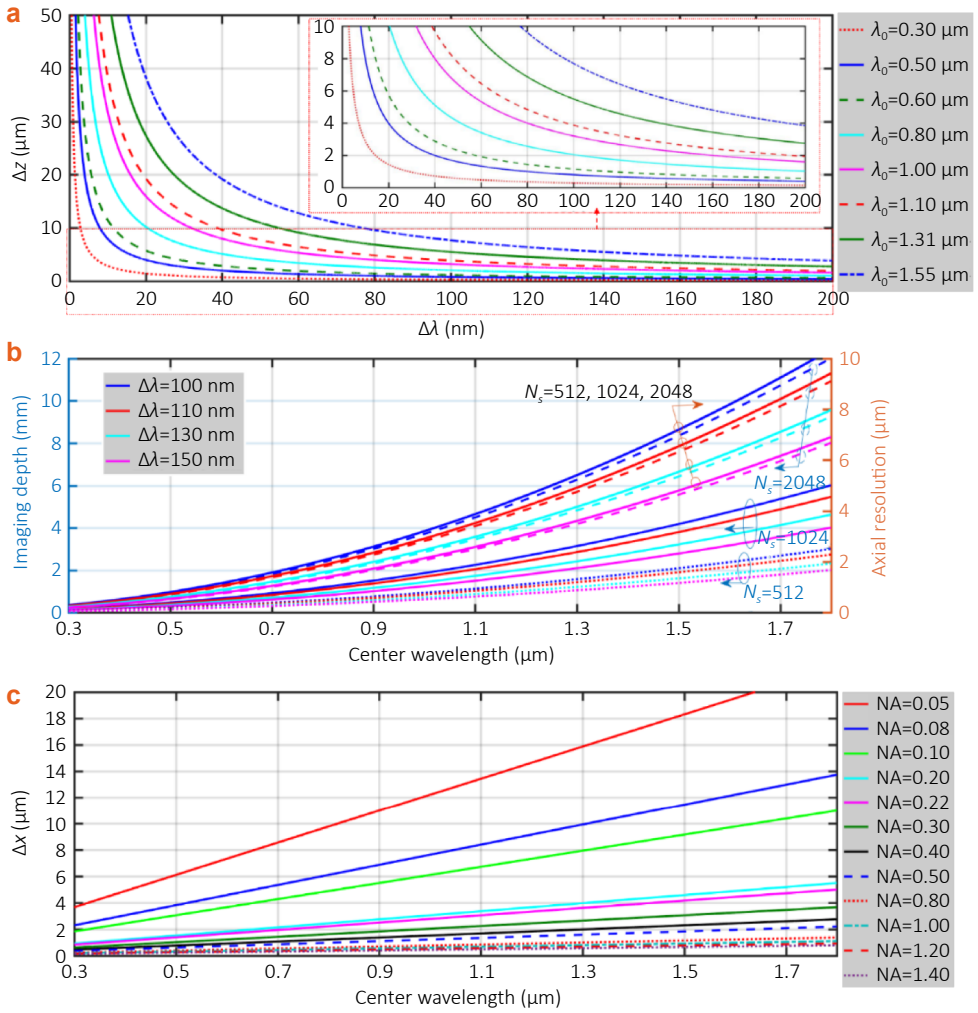

Fig. 3 | The axial resolution Δ*z*, imaging depth, and lateral resolution Δ*x* of OCT. (a) For a certain central wavelength λ_0, indicating axial resolution Δ*z* as a function of optical bandwidth Δλ with n_s = 1.38. (b) For certain optical bandwidths Δλ, indicating the maximum imaging depth and axial resolution Δ*z* of OCT as a function of central wavelength λ_0 with n_s = 1.38 and sampling point numbers of N_s=1024, N_s = 2048, and N_s = 512, respectively. (c) For certain NAs indicating lateral resolutions Δ*x* of OCT as a function of the central wavelength λ_0.

tissue (from scattering and absorption) ultimately limits how deep OCT can actually visualize; most biological tissues allow imaging on the order of 1mm-3 mm deep, depending on wavelength and sample tissue.

The lateral resolution (Δ*x*) refers to the smallest transverse detail that can be resolved, and it is determined by the focusing optics in the probe. For a diffraction-limited Gaussian beam, lateral resolution can be expressed as

$$\Delta x = \frac{4\lambda_0}{\pi}\frac{f_0}{d}, \tag{3}$$

where f_0 is the focal length of the objective lens (or fiber), and d is the effective beam diameter on that lens. In practice, lateral resolution (Δ*x*) is governed by the numerical aperture (NA) of the focusing optics; a higher NA (larger beam diameter or shorter focal length) yields a smaller spot and thus better lateral resolution. Figure 3(c) shows that for a given NA, the Δ*x* becomes poorer (larger spot size) at longer wavelengths. It also shows that increasing the NA improves Δ*x*. For example, using a shorter wavelength or a larger NA lens will decrease Δ*x*. However, a higher NA also means a smaller depth of focus, so the high lateral resolution is maintained only over a smaller range in depth. In summary, lateral resolution improves with higher NA and shorter wavelength, at the expense of reduced depth of field.

It is often challenging to simultaneously maximize axial resolution, lateral resolution, imaging depth, and field of view. There is an inherent trade-off between depth resolution and depth range—using a broad bandwidth light source to achieve ultrahigh axial resolution inherently shortens the effective imaging range due to spectrometer limitations and increased dispersion. Similarly, using a high-NA lens to sharpen lateral resolution reduces the depth of focus and overall field of view. These trade-offs mean that the OCT system design must be optimized for the target application.

Many clinical applications (for example, detecting early-stage cancers or precancerous lesions) benefit from both high axial and high lateral resolution, since such fine detail is needed to spot subtle abnormalities. Therefore, advanced optical techniques are employed to push these limits.

To extend the depth of focus without sacrificing lateral resolution, researchers have experimented with wavefront engineering. For instance, Li et al. designed a wavefront-coded microscope employing specially designed phase masks (both non-symmetric and symmetric) in the optical path. This approach extended the depth of field to approximately 13× greater than a traditional imaging system[31,32]. Additionally, Li et al. also reported an adaptive objective lens that maintains near-diffraction-limited focusing over a wide range of depths for ultra-broadband NIR OCT imaging[33,34]. By incorporating an embedded tunable lens into the objective, they kept the lateral spot size nearly constant over a broad focus range. This design, calculated at an 800 nm central wavelength, achieved a consistent lateral resolution of ~2.2 μm-2.8 μm across the imaging depth (NA varying from 0.214 to 0.171 over the range)[33]. Wavefront-engineering for endoscopic OCT has been investigated with metasurface-enabled optics. In 2018, Pahlevaninezhad et al. demonstrated an endoscope integrated with a nano-optic metalens at the catheter tip to correct non-chromatic aberrations and, critically, to exploit tailored chromatic dispersion in spectral interferometry. This maintained near-diffraction-limited lateral resolution beyond the Rayleigh range without additional computational burden, and was validated in-vivo in sheep airways and ex-vivo in human lung imaging[35]. More recently, Pahlevaninezhad et al. introduced bijective illumination–collection imaging, which decouples lateral resolution from depth of focus by establishing a one-to-one mapping along a focal line using metasurface, achieving ~3.2 μm lateral resolution at 1.3 μm wavelength sustained over ~1.25 mm depth of focus with standard OCT acquisition and reconstruction[36]. These results show that metasurface phase control can simultaneously address catheter-induced aberrations and the resolution–depth of focus (DOF) trade-off in ultrathin OCT probes, pointing to a practical pathway for high-NA, long-DOF endoscopic tomography.

Another crucial aspect for endoscopic OCT is real-time imaging and motion correction. In 2022, Lyu et al. developed a high-speed imaging platform for endoscopic SS-OCT that combined GPU (CUDA) processing with a field-programmable gate array (FPGA)-based data acquisition and synchronization scheme[37]. They optimized memory usage with a half-synchronous/half-asynchronous data handling mode and used an asynchronous streaming architecture to multiplex multiple processing threads at high speed. In addition, a rotary encoding feedback module was added to the probe's motor, which provided 25 ns precision timing synchronization via an FPGA clock (40 MHz), thereby suppressing image distortions from non-uniform rotation. Using this system, they achieved an A-scan processing rate of 3.52 MHz (for 1024-pixel depth, 16-bit data), including memory transfers and real-time display. This corresponds to a B-scan frame rate of 200 frames per second (fps) (1024×1024 pixels), which they demonstrated by imaging a mouse esophagus and human fingertip with stable, high-quality output at 200 fps.

Finally, the signal-to-noise ratio (SNR) of the system has a significant impact on image quality. A higher SNR enables the detection of weaker reflections and reveals fine structures with better contrast against noise. High-performance OCT systems typically achieve SNR above 100 dB, meaning they can detect reflected OCT optical signals as weak as 10^{-10} of the incident optical power. Attaining such a high SNR involves optimizing the optical throughput (minimizing losses), using sensitive detectors, and employing a stable, low-noise light source. As an example of this aspect, Li et al. introduced a k-space spectrometer design for SD-OCT that improved the sensitivity and contrast for imaging deeper tissue[38]. In designing OCT endoscopes, practical factors like compactness, flexibility, ease of use, and cost must be balanced with these performance metrics. The ultimate goal is to reliably visualize microscopic morphology in vivo, which often requires a combination of the above improvements.

2.3 OCT endoscopic probes and recent advances

The OCT endoscopic imaging system can be constructed using fibers, waveguides, and other micro-optical components. These components can be integrated into catheters or endoscopes to capture high-resolution images of the microstructure of internal organs. Essentially, an OCT endoscopic system aims to focus an imaging beam onto the sample, scan it, collect the back-reflected light from the sample, and transmit the data back to the detector of the OCT endoscopic system. Early OCT endoscopy research began in the 1990s. In 1997, Tearney et al. reported the first in vivo endoscopic OCT images, using a catheter-based OCT probe about 1 mm in diameter[4]. They obtained cross-sectional images of a rabbit's gastrointestinal and respiratory tracts with a resolution of 10 μm[4]. Since then, a wide variety of OCT endoscopic probes have been developed for different clinical applications.

OCT endoscopes are typically categorized into side-viewing and forward-viewing types, depending on the direction of the imaging beam. Side-viewing endoscopes, where the beam emerges laterally, are ideal for imaging the walls of luminal organs over a wide area, while forward-viewing endoscopes, where the beam emerges at the tip, are more suitable for guiding biopsies or interventions. Most OCT probes for tubular organs (esophagus, blood vessels, airways, etc.) are side-viewing, since they can scan the circumference as they are pulled back.

For side-viewing endoscopes, there are two subtypes based on the location of the beam-scanning device: proximal-

Table 1 | Comparison between the proximal-end and the distal-end scanning OCT endoscopes. Reproduced with permission.[39]Copyright 2017, The Optical Society.

Scanning type	Min. prober dia. (φ) and rigid length (L)	Max. speed	Imaging area	Fiber stress-induced distortion	Expense
Proximal- scanning	~0.5 mm (φ)~1.0 cm (L)	~0.2k rps	Large (with pullback)	Moderate	Low (disposable)
Distal-scanning	~1.5 mm (φ)~2.0 cm (L)	~4k rps	Large (with pullback)	Less	High (with micromotor)

end scanning probes and distal-end scanning probes. In proximal-end scanning probes, the optical fiber itself is rotated (and often pulled back) from the console side using a rotating torque cable. In distal-end scanning probes, a tiny micro-motor at the tip of the probe directs the beam. Each approach has pros and cons; a comparison between these two types is summarized in Table 1[39]. From Table 1, we can see that proximal-end scanning probes can be very thin (probe diameter ~0.5 mm and rigid tip length ~10 mm) since only a fiber and simple optics are at the tip. They are also relatively cost-effective and can be disposable. However, rotation speed is limited (on the order of 0.2 k rps) due to torque cable dynamics, and the image quality may suffer from fiber winding and non-uniform rotation, which can introduce distortions (stress on the fiber during rotation can change its refractive index slightly). Distal-end scanning probes incorporate a small motor and optics in the tip, resulting in a larger probe diameter (~1.5 mm, rigid length ~20 mm) and higher cost. The advantage is a much higher rotation speed (several k rps is possible, e.g., ~4 k rps) and more uniform scanning, since the fiber isn't continuously twisted along its length. Distal scanners also minimize the rotational torsion on the fiber, reducing signal distortion. The trade-off is a thicker probe and increased complexity (needing electrical connections for the motor).

Both types of side-viewing endoscopy probes typically use a rotating sheath or torque coil around the fiber for stability and to allow pullback motion. This distal optics (like a microprism or mirror and a focusing lens) is enclosed in a protective transparent sheath (often a polymer tube) to prevent direct contact with tissue and fluids. The sheath permits sterilization and reduces friction during rotation. However, a side-viewing endoscope with a transparent protective plastic tube can distort a round-shaped imaging beam into an elliptical one. This distortion leads to a significant loss of resolution and uneven focus[40]. To address this, Xi et al. developed a new optical design for an OCT balloon imaging catheter[41]. They replaced the standard flat reflector with a curved reflector, designed with a pre-calculated surface curvature, to achieve higher resolution at a significant working distance. This design also corrects severe astigmatism in the catheter[41]. The design incorporated a 1 mm diameter gradient-index lens with an appropriately chosen pitch number and a glass rod spacer to fully utilize the available numerical aperture (NA). The catheter based on this new design achieved a diffraction-limited lateral resolution of approximately 21 μm, a working distance of ~11 μm-12 μm, and a round-shaped beam profile.

In the aspect of rotational scanning and pullback, modern OCT endoscopic probes generally use a rotation-plus-pullback scanning method to generate 3D images of hollow structures (e.g., arteries, airways, or the digestive tract). A motor spins the fiber or the distal optics to produce a circular scan (B-scan) of the tissue, and simultaneously the probe is translated longitudinally (pullback) to stack these slices into a 3D volume. This scanning mechanism yields a cylindrical dataset of the organ's inner lining. These probes are typically made from optical fibers and are driven from the proximal end using rotary motors to transmit the rotary motion to the distal imaging probe. The distal imaging probe utilizes a stepwise transitional core structure instead of a focusing lens to narrow the light and enhance lateral resolution.

In some ultra-thin probe designs, the usual focusing lens is omitted to keep the probe diameter minimal. For example, Moon et al. proposed an ultra-thin and flexible endoscopic OCT probe in 2015 for imaging the small airways of rabbits. Their probe was built from an 85 μm diameter fiber within a protective tubing of only 160 μm thick[42]. It used a stepwise transitional core fiber section to deliver OCT light through a single-mode fiber and expand the beam to a 24 μm mode field diameter, which significantly reduced beam divergence even without a lens. The distal end face of the optical fiber is polished at ~43° - 47° to internally reflect the beam sideways (similar to a prism) and direct it into the tissue. By slightly offsetting the angle from exactly 45°, back-reflections from the fiber cladding and sheath surface into the fiber were minimized. Despite its tiny size, this probe could acquire cross-sectional OCT images with a lateral resolution of ~24 μm. Moon's group demonstrated the probe by imaging a rabbit's airway ex vivo, showing that even very narrow lumens could be accessed with OCT. Building on this concept, Chen et al. in 2018 used a similar ultra-thin probe to perform in vivo imaging of rat airways in a toxic gas inhalation injury model[43]. The probe was connected to an external rotational motor, rotating at 1500 rpm to acquire 2D images at 25 frames per second (fps). It was pulled back at a constant speed of 5 mm/s along the airway to obtain 3D scans of the rat trachea. The axial and lateral resolutions of the probe were ~6.8 μm and ~34 μm in air, respectively[43]. These ultra-flexible, lens-free probes illustrate how miniaturization can be pushed to visualize delicate structures like small bronchi, though often at the cost of some resolution and signal strength. Miniaturized endoscopic probes are essential for imaging small luminal organs or delicate tissues without causing damage. However, current fabrication

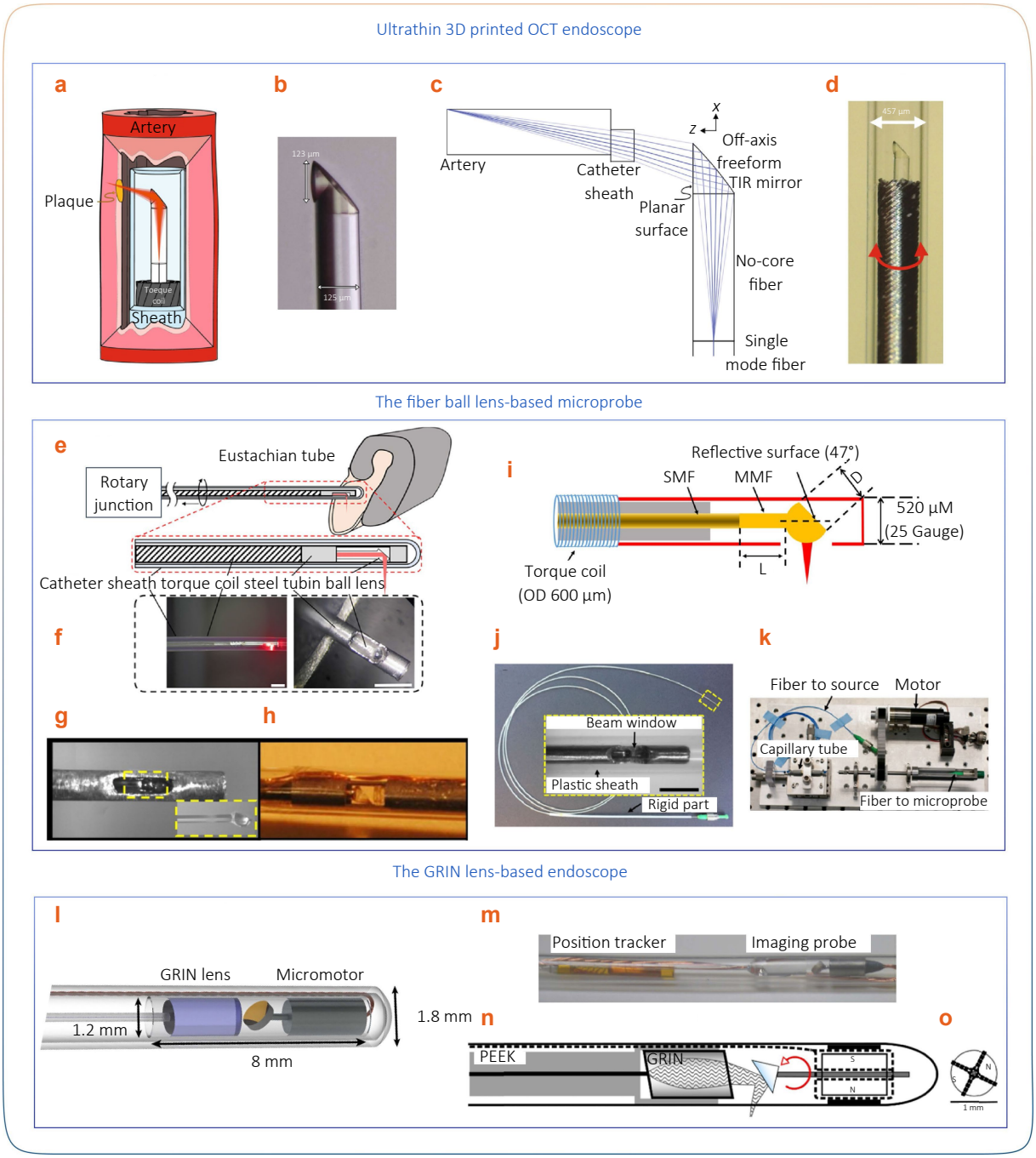

Fig. 4 | (a-d) Ultrathin 3D printed OCT endoscope design. Reproduced under the terms of a CC-BY license.[44]Copyright 2020. The Authors. Published by Springer Nature. (a) Schematic of the 3D printed OCT endoscope inside an artery; (b) Microscope image of the 3D printed off-axis freeform total internal reflection mirror on the tip of the no-core fiber (NCF) that is fusion spliced onto the light-guiding SMF; (**c**) Optical design of the system with light exiting the SMF, expanding in the NCF, being reflected and phase-shaped at the freeform mirror, passing the catheter sheath and focusing into the artery tissue; (d) Photo of the 3D printed OCT endoscope, which rotates and is pull back to accomplish full 3D OCT scanning. (e) and (f) Photographs of an SS-OCT endoscopic probe. Reproduced under the terms of a CC-BY license[52].Copyright 2021. The Authors. Published by Springer Nature. (g) and (h) Photograph of microprobe, which consists of a fiber ball-lens in the 25-gauge protective tube, inset: zoomed-in view of fiber ball-lens. Reproduced with permission.[56]Copyright 2016, Elsevier. (i-k) Schematic of the fiber ball lens-based microprobe. Reproduced under the terms of a CC-BY license.[19]Copyright 2017. The Authors. Published by Springer Nature. (i) The design of a microprobe encased within a transparent plastic sheath of a 1 mm outer diameter. (j) An equivalent forward-viewing design of a microprobe. (k) Experimental setup and microprobe prototype with a rotary joint consisting of a glass capillary tube. (l, m) Fully integrated OCT imaging probe and position tracker. Reproduced under the terms of a CC-BY license[60]Copyright 2016. The Authors. Published by Springer Nature. (n, o) Schematic and cross-section of the OCT endoscope. Reproduced with permission.[21]Copyright 2019, The Optical Society.

methods impose limitations on the imaging performance of these highly miniaturized probes, hindering their widespread use. To address this challenge, in 2020, Li et al. developed a novel ultrathin probe fabrication technique that utilizes 3D microprinting to reliably create side-facing, freeform micro-optics (<130 μm diameter) on single-mode fibers[44]. The smallest 3D imaging probe reported to date, with a diameter of 0.457 mm (including the catheter sheath), is shown in Fig. 4(a-d). This probe represents the cutting edge of miniaturization in OCT technology. Li et al. demonstrated its imaging quality and mechanical flexibility by successfully imaging atherosclerotic arteries in humans and mice[44].

As preclinical and clinical diagnostics increasingly rely on techniques for visualizing internal organs at high resolution via endoscopes, these innovations are key to advancing diagnostic capabilities. Achieving higher resolution in OCT endoscopy has also been a focus of research. Standard clinical OCT systems have resolutions on the order of 5 μm-10 μm. By using ultra-broadband light sources and carefully engineered optics, micro-OCT (μOCT) systems can reach ~1 μm-3 μm resolution. Tearney et al. developed an SD-μOCT that integrates a next-generation ultra-broadband supercontinuum light source with an engineered beam shape, achieving lateral resolution of 2 μm, axial resolution of 1 μm, and a depth of focus of 300 μm. This technology was first demonstrated in ex vivo human coronary artery plaques[45], revealing microscopic structural details of atherosclerosis beyond what standard OCT could see. Additionally, to adapt μOCT for airway imaging, the same group designed a 4 mm diameter rigid endoscopic probe that utilized gradient-index focusing optics and a selectively coated prism reflector to implement circular-obscuration apodization, enhancing the depth of focus. With this probe, they obtained high-resolution μOCT images of the tracheal epithelium in living swine. Benchtop characterization showed 3.4 μm lateral and 1.7 μm axial resolutions in tissue for the probe, slightly lower than the full μOCT due to the constraints of the probe optics. During imaging, they inflated a small balloon around the probe to stabilize it against the airway wall and reduce motion[46]. This work demonstrated that near-microscopic resolution OCT is attainable in an endoscopic format, enabling visualization of the structures, cilia, and glands in the airway epithelium.

Another notable development for extended imaging range is the work by Oldenburg et al., who introduced a quantitative upper airway endoscopy system using SS-OCT that employed a specially designed swept light source with a very long coherence length (17.5 mm)[47]. This system also featured a custom fiber-optic catheter capable of providing a prolonged (>10 mm) imaging range. The catheter included an angle-polished ball lens at the tip, housed in an 820 μm outer diameter sheath, making it suitable for the 1.2 mm channel of commercially available flexible pediatric endoscopes. It was successfully used for long-range reconstructions of human airway phantoms and ex vivo swine trachea. In 2017, Xie et al. proposed and fabricated a prototype focus-adjustable endoscopic probe based on a two-way single-mode fiber (SMF) spring and a homemade hollow-core ultrasonic motor. Unlike traditional DOF-extended probes, this focus-adjustable probe had an adjustable focus, a larger scanning range, high resolution, and no sensitivity loss. They demonstrated C-mode scanning in endoscopic OCT with a lateral resolution of ~4 μm and a DOF of only 160 μm. The focus-adjustable probe enabled a depth-scanning range of 1.5 mm with high resolution and no sensitivity loss. A homemade hollow-core ultrasonic motor facilitated unobstructed 360° distal scanning[48].

For in vivo airway imaging, the primary limitation of OCT imaging in small animal airway studies is the probe diameter, which is constrained by the average healthy rat trachea diameter of approximately 2.8 mm. Delacrétaz et al. introduced an endoscopic OCT system in 2009 to visualize the topology of the upper airways through rigid endoscopes[49]. In 2016, Li et al. reported an ultrahigh-resolution, high-speed distal scanning SD-OCT endoscope for small airway imaging. The system achieved an axial resolution of 2.6 μm at 20 frames per second in the small sheep, enabling detailed in-vivo 3D assessment of the bronchial structures[50]. At the same time, OCT provided cross-sectional images of tissue structures, such as cilia movement and mucus secretion, it lacked sufficient contrast to differentiate individual cells. However, fast sequences of microscopic-resolution OCT images helped overcome contrast limitations and speckle noise, enabling visualization of airway morphology at the cellular level and tracking dynamic behavior of immune cells, as well as transport and secretion[51]. In 2022, Kohlfaerber et al. demonstrated that microscopic-resolution OCT allowed the study of physiological and pathological tissue processes in vivo, using temporal tissue fluctuations as a contrast mechanism[51]. Toxic gas inhalation often leads to airway obstruction and narrowing, making it difficult for most endoscopic OCT probes to pass through. Therefore, designing a flexible, side-scanning, ultra-small OCT probe becomes crucial. In 2017, Li et al. reported an ultracompact microprobe with a diameter of 520 μm and a rigid length of 5 mm. The super-achromatic probe featured a built-in monolithic fiber-optic ball lens, which achieved an ultrahigh axial resolution of 1.7 μm in tissue and 6 μm lateral resolution at 800 nm[19], as shown in Fig. 4(i). The microprobe was simple to fabricate, consisting of a homemade fiber ball lens and a short piece of multimode fiber (MMF) as a spacer (or beam expander) spliced to a single-mode fiber (SMF). The fiber ball lens was designed with a reflective surface at 47°, deflecting the imaging beam for side-viewing and avoiding potential high back-reflection from the protective plastic sheath surrounding the entire microprobe and tissue surface. A photograph of the 2-meter-long flexible microprobe encased in a transparent protective plastic sheath is shown in Fig. 4(j). Imaging beam rotation

was performed at approximately 5 fps using a homemade glass capillary-based rotary joint, as shown in Fig. 4(k). The endoscopic OCT performance and translational potential were demonstrated through in vivo imaging of a mouse colon, rat esophagus, and small airways in sheep.

Beyond the airways, OCT endoscopy has been applied to other organ systems with unique challenges. The Eustachian tube, for example, is a narrow passage connecting the middle ear to the throat. In 2021, Byun et al. developed a specialized side-viewing OCT catheter to image the Eustachian tube[52]. To enhance both resolution and OCT penetration depth, they chose a catheter sheath made of fluorinated ethylene propylene (FEP), a material with a refractive index of 1.33, which is closer to that of water compared to Pebax (refractive index of 1.508), a commonly used material in coronary artery imaging. This design improved transmission and reduced image distortion. The new Eustachian OCT catheter was successfully inserted into the tubal lumen without causing damage. A schematic of the SS-OCT endoscopic imaging system is shown in Fig. 4(e). The specialized round-tipped OCT catheter was fabricated with a catheter sheath having an outer diameter of 1.01 mm and an inner diameter of 0.71 mm, as shown in Fig. 4(f). It achieved ~8.3 μm axial resolution and ~22.7 μm lateral resolution, with a pullback scan range of 35 mm-45 mm. Using an SS-OCT, they obtained real-time images at 50 frames/s while a pullback speed of 3 mm/s, successfully visualizing the tubal lumen[52]. Another delicate area is the inner ear. In 2021, Tearney et al. demonstrated that μOCT could image the inner ear's sensory epithelium in cadaveric human inner ears[53]. This application is highly challenging due to the small size and fragility of the inner ear structure, but OCT's label-free nature and high resolution make it a promising tool for cochlear imaging, potentially aiding in the study of hearing loss if adapted for live use.

In the gastrointestinal tract, OCT has been explored as a complementary imaging modality during endoscopy. A notable example is the use of OCT to image the pancreatic and bile ducts. Singh et al. performed the first in vivo OCT imaging of the pancreatic ductal system in dogs using a side-viewing OCT catheter inserted through an endoscope into the pancreatic and biliary ducts[54]. Their findings revealed that OCT images correlated well with histological results, suggesting that OCT could aid in identifying abnormal ductal epithelium. However, a practical challenge is that contacting the delicate duct walls with the probe can compress the tissue, and excessive pressure can flatten the epithelium, altering its appearance[54,55]. To mitigate this, a gentle contact or slight standoff is needed. While a bit of pressure can increase imaging depth, it must be carefully controlled to avoid distorting the tissue microanatomy. Furthermore, accessing the biliary duct endoscopically requires navigating the duodenoscope through multiple sharp bends of the duodenum, necessitating ultra-flexible probes with a small diameter.

To address these challenges, Yuan et al. in 2021 proposed an ultrahigh-resolution endoscopic OCT system with an axial resolution of 2.4 μm. The system included a distal-scanning probe with an outer diameter of approximately 1.8 mm (with protective plastic sheaths) and a microprobe with an outer diameter of around 1 mm, both housed in protective sheaths, as shown in Fig. 4(g,h)[56]. The development of high-resolution, label-free imaging techniques for in vivo pathology detection during colonoscopy is crucial for early disease detection and accurate biopsies. Colonoscopic OCT has been used to visualize colonic microstructures beneath the mucosal surface. However, its clinical application remains limited by sub-optimal resolution (~6.5 μm in tissue), inadequate imaging contrast, and the absence of high-resolution OCT criteria for lesion detection. In 2022, Li et al. introduced an ultrahigh-resolution colonoscopic OCT system and evaluated its capabilities for visualizing and identifying the pathological features of inflammatory bowel disease in a rat model. With improved resolution (~1.7 μm in tissue) and enhanced contrast, the system accurately delineated fine colonic microstructures and identified the pathophysiological characteristics of inflammatory bowel disease in vivo[57].

OCT endoscopy provides high-resolution images of the gastrointestinal (GI) mucosa and submucosa, but it remains uncertain whether it can reliably detect dysplasia in GI tissue. To investigate this, Pfau et al. studied colon polyps, comparing OCT imaging features of colon polyps with normal colon tissue. The study demonstrated that OCT imaging could differentiate adenomas, hyperplastic polyps, and normal colon tissue in real-time. Specifically, dysplasia in colon adenomas appeared as a loss of tissue organization and reduced light scattering[58].

High-speed imaging significantly enhances diagnostic accuracy by capturing subtle changes and dynamic processes in real-time. It reduces patient discomfort during examinations, minimizes motion-induced image blurring, and improves the efficiency of healthcare professionals, leading to more timely diagnoses and better treatment and monitoring outcomes. In 2014, Tsai et al. described an ultrahigh-speed endoscopic SS-OCT system for clinical gastroenterology utilizing a vertical-cavity surface-emitting laser (VCSEL) and a micromotor imaging catheter. This system achieved an axial scan rate of 600 kHz, an axial resolution of 8 μm in tissue, and an imaging rate of 400 fps (24,000 rpm) with a pullback speed of 2 mm/s and a 12 μm spot size, using a catheter with a 3.2 mm outer diameter and an 18.2 mm rigid length. The total length of the torque coil and sheath for the prototype catheter was approximately 2 meters[59]. In 2016, Chen et al. proposed a long-range OCT system that integrated high-speed imaging with a real-time position tracker, enabling the acquisition of accurate 3D anatomical structures in vivo. The system achieved an imaging range of 30 mm at a frame rate of 200 Hz, allowing for rapid, comprehensive visualization and quantification of the

airway, the long-range imaging catheter, shown in Fig. 4(l) and 4(m)[60]. This development highlights the increasing importance of high-resolution visualization techniques in preclinical and clinical diagnostics of internal organs via endoscopes. Although endoscopic OCT can achieve high imaging speeds, limitations in the speed of optical rotation or OCT acquisition rates can still affect overall imaging speed. To address this, Tsai et al. developed a piezoelectric-transducer (PZT)-based miniature catheter with an outer diameter of 3.5 mm for ultrahigh-speed endoscopic OCT. This system achieved an axial resolution of 11 μm in air (8 μm in tissue) and a lateral resolution of 20 μm, with imaging performed at 960 fps using a Fourier domain mode-locked laser (FDML) operating at a 480 kHz axial scan rate. The system's sensitivity was measured at 103 dB, with an imaging depth range of 2.3 mm in air (1.7 mm in tissue), and the sensitivity decreased by approximately 7.5 dB at an imaging depth of 2.25 mm. They successfully demonstrated the endoscopic OCT imaging of a rabbit's esophagus and colon in vivo, as well as human colon specimens ex vivo[61]. To achieve uniform data acquisition in the frequency domain, Li et al. in 2010 also introduced a real-time, universal K-space sampling method for a high-speed SS-OCT system, based on an FDML with a 40 kHz axial scan rate. This system achieved an axial resolution of 9.3 μm and detection sensitivity greater than 120 dB[62]. Most OCT endoscopic instruments are side-viewing and rely on at least one proximal scan, which limits the accuracy of volumetric imaging and enface visualization. To overcome this, Fujimoto et al. in 2017 proposed a forward-viewing fiber scanning 3D-OCT probe, with a 3.3 mm diameter, 20 mm rigid length, 900 μm field of view (FOV), and 5 μm lateral resolution, imaging at a 1 MHz axial scan rate within the human gastrointestinal tract[63]. A wide FOV is crucial for endoscopic assessments and diagnoses of luminal organ diseases, such as those encountered in gastroenterology. In 2018, Fujimoto et al. demonstrated a new cycloid scanner integrated into a tethered capsule for ultrahigh-speed, side-viewing OCT endomicroscopy in vivo. This capsule incorporated two scanners: a piezoelectrically actuated resonant fiber scanner for fast scanning with precise, small FOV, and a micromotor scanner for slow scanning with a wide FOV. Together, these scanners performed circumferential beam scanning in a 2D cycloid pattern, producing an unwrapped 1 mm × 38 mm strip FOV. Sequential strip volumes were acquired via proximal pullback to image centimeter-long regions. Using ultrahigh-speed 1.3 μm wavelength SS-OCT at a 1.17 MHz axial scan rate, they imaged the human rectum at 3 volumes per second, with an axial resolution of 8.5 μm and a lateral resolution of 30 μm[64].

Maintaining ultrahigh axial resolution is crucial, and one challenge is preserving the broad spectral bandwidth of the light source throughout the OCT system. To overcome this, Li et al. presented the first compact, ultrahigh-resolution, high-speed distal scanning OCT endoscope operating at 800 nm in 2018. This system utilized diffractive optics to minimize spectral throughput loss. A customized miniature 900 μm diameter DC micromotor fitted with a micro-reflector scanned the imaging beam[65], however, in OCT endoscopy, a fiber catheter with side-viewing optics is typically connected proximally to a rotary joint. This setup allows the catheter to rotate independently of the rest of the system, facilitating the measurement of sample retardance. However, this configuration can distort the optical axis of the sample due to the polarization effects in the system[66]. Accurately assessing the optical axis of birefringent tissue could significantly aid in differentiating and characterizing various tissues. Unfortunately, the distortion caused by the system has previously prevented the precise measurement of the sample optical axis.

To address this, Suter et al. introduced a simple calibration technique in 2018 to recover the sample OA[67]. This innovation enabled more accurate polarization-sensitive measurements. In 2019, de Boer et al. introduced a custom motorized OCT probe[21], as shown in Fig. 4(n) and 4(o). By utilizing OA uniformity, they were able to highlight the presence of uniformly arranged fiber-like tissue, thus visualizing the abundance of airway smooth muscle and connective tissue structures. Their attenuation coefficient images of airways, which were presented for the first time, demonstrated superior architectural contrast compared to standard OCT images[21]. In 2021, de Boer et al. utilized polarization-sensitive OCT (PS-OCT) to image healthy and diseased lungs ex vivo, identifying differences in alveolar size and airway smooth muscle thickness[68]. While incorporating polarization sensitivity into OCT greatly enhances its ability to differentiate various tissue types based on intrinsic contrast, polarization mode dispersion (PMD) can significantly hinder the accuracy of polarization data, unless the system sacrifices axial resolution. To address this challenge, in 2022, Adams et al. proposed a novel technique to compensate for PMD in endoscopic PS-OCT, minimizing the impact on axial resolution and enabling more accurate polarization data without requiring coherent polarization inputs. Instead, it requires only a birefringent structure with a known orientation in view —such as the catheter sheath—making it more practical for clinical applications[69].

The field of OCT endoscopy is rapidly advancing, driven by innovations in light sources, optical design, and miniaturization. Functional OCT methods (like Doppler, polarization-sensitive, and angiographic OCT) add rich contrast to the structural images, aiding early disease detection. At the same time, improvements in resolution (both axial and lateral), imaging speed, and probe design are expanding the capabilities of endoscopic OCT. From ultra-fast imaging systems to ultra-small probes and high-resolution microscopes inside needles, these developments are bringing OCT closer to fulfilling its promise of providing clinicians with real-time, microscopic views of tissue architecture in vivo. Each new advancement in hardware or computational

imaging helps bridge the gap between what can be achieved with noninvasive optics and the gold standard of histopathology, with the ultimate goal of enabling earlier and more accurate disease diagnosis.

Despite the significant progress in OCT endoscopy in the biomedical field, the high cost of OCT systems has hindered widespread clinical adoption. To address this, new technological approaches are necessary. Integrated optical technology is emerging as a promising solution. Integrated optics simplifies systems, reduces size, improves image quality, and lower costs. By integrating traditional optical components into a chip, these technologies enable the creation of compact, reliable imaging systems. The following section will provide an overview of the status of on-chip integrated optics, particularly focusing on on-chip optical detectors and light sources, which are crucial for advancing on-chip OCT development.

3 Integrated optics on a chip

The development of fully integrated on-chip OCT systems represents a critical milestone in the evolution of optical imaging technologies. Central to this achievement is advances in on-chip light sources and detectors, driven by rapid progress in photonics and semiconductor technologies. These innovations have enabled the creation of compact, cost-effective OCT systems, paving the way for their broader application in medical diagnostics, biological imaging, and other fields. Furthermore, all the integrated-optics devices, such as light sources, photodetectors active optical components, can be exploited for endoscopic and non-endoscopic OCT systems and enable more compact designs and implementations.

4 Monolithic integration of light sources

In 2012, Tilma et al. proposed the first monolithically integrated tunable laser for OCT, incorporating passive components, phase modulators, and quantum-dot amplifiers. The tunable laser demonstrated electro-optical tuning capabilities over a 60 nm range (1685 nm to 1745 nm) with an effective linewidth of 0.11 nm and an output power of approximately 0.1 mW. The laser was scanned over this range in 4000 steps at a scan frequency of 500 Hz, with wavelength switching occurring within 500 ns[70]. This breakthrough laid the foundation for compact, tunable light sources necessary for integrated optics-based OCT systems. The direct monolithic integration of III-V lasers on silicon substrates has been particularly challenging due to lattice mismatches and differing thermal expansion coefficients between the materials. In 2016, Chen et al. developed the first InAs/GaAs quantum-dot lasers grown directly on silicon substrates, as

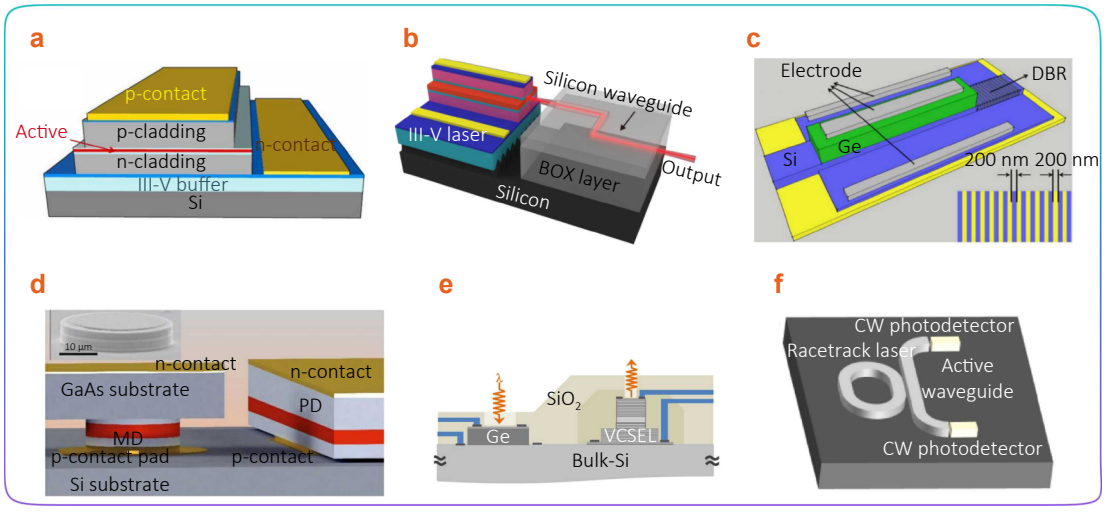

Fig. 5 | Schematic diagram of an on-chip laser and detector. (a) Schematic of the layer structure of an InAs/GaAs QD laser on a silicon substrate. Reproduced with permission.[71]Copyright 2016, The Authors. Published by Springer Nature. (b) Schematic of monolithic integration of III-V QD laser edge coupled with silicon waveguide on SOI platform. Reproduced under the terms of a CC-BY license.[77]Copyright 2023, The Authors. Published by Springer Nature. (c) 3D schematic structure of the germanium photodetectors integrated on top of the SOI waveguide with the distributed Bragg reflector (DBR). The inset shows a structural diagram of the DBR. Reproduced with permission.[78]Copyright 2017, The Optical Society. (d) Schematics of the microlaser and PD bonded on Si substrate. Inset: scanning electron microscopy image of the initial microdisk (MD) laser. Reproduced with permission.[79]Copyright 2004, Published by IOP Publishing. (e) Schematic diagram of monolith-integrated TRx devices on bulk silicon wafer, this can be an integrated photonic I/O platform for major electronic chips based on bulk silicon, or compact single-chip photonic transceivers for network applications. Reproduced under the terms of a CC-BY license.[80]Copyright 2015, The Authors. Published by Springer Nature. (f) A racetrack quantum cascade laser (QCL) with an evanescently coupled waveguide, which allows for outcoupling of light, and photodetectors were fabricated on each end of the waveguide to then capture this signal. Reproduced with permission.[81]Copyright 2022, The Optical Society.

shown in Fig. 5(a), achieving room-temperature output powers exceeding 105 mW, low threshold current densities (62.5 A/cm^2), and operational capabilities up to 120 °C[71]. This advancement in quantum-dot laser technology on silicon substrates represents a significant step toward integrating high-performance light sources on-chip. In 2017, Thourhout et al. demonstrated InGaAs/GaAs single-mode nano-ridge lasers directly on a standard 300-mm Si wafer, using defect-trapping techniques to achieve single-mode lasing and side-mode suppression exceeding 28 dB[72]. This approach showcased the potential of integrating high-quality III-V materials onto CMOS-compatible Si platforms for future photonic applications, such as dense wavelength division multiplexing (DWDM) in telecommunications. In 2018, Zhu et al. reported the first InGaAs/InAlGaAs multi-quantum-well (MQW) lasers grown directly on on-axis V-grooved Si substrates by metalorganic chemical vapor deposition (MOCVD). These lasers exhibited lasing near 1.5 μm, with a threshold current density of J_{th} = 3.3 kA/cm^2 under pulsed current injection at room temperature[73].

A major challenge in integrated photonics has been the direct monolithic integration of III-V materials like indium phosphide (InP) on silicon substrates. In 2019, Hu et al. proposed a solution involving III/V-on-Si MQW lasers fabricated by regrowth on a bonding template, addressing lattice, thermal, and domain mismatch issues typical in heteroepitaxy processes. These lasers[74] demonstrated room-temperature pulsed and continuous-wave lasing at 1.31 μm with a minimal threshold current density of 813 A/cm^2. This breakthrough significantly advanced the development of scalable, cost-effective light sources for on-chip integrated optics. In 2020, Haindl et al. introduced an ultra-high-resolution SD-OCM imaging system with a compact polarization-aligned 840 nm broadband combined-SLED source. This source provided an optical bandwidth of 160 nm and an output power of 12 mW, with three superluminescent diodes (SLEDs) integrated into a 14-pin butterfly module using a free-space micro-optical bench architecture, while maintaining a constant polarization state across the full spectral output[75]. In 2021, Yan et al. proposed a monolithic InP-on-SOI platform to combine the benefits of both silicon photonics and InP photonics. Through the selective growth of InP sub-micron wires and large-dimensional InP membranes on industry-standard Si wafers, they achieved site-controlled epitaxial InP that was dislocation-free. This breakthrough enabled the realization of various photonic functionalities while efficiently interfacing III-V devices with Si-based waveguides, advancing the development of fully-integrated Si-based photonic integrated circuits (PICs)[76].

Achieving the monolithic integration of III-V lasers with silicon photonic components on a single silicon wafer has long been a significant challenge for ultra-dense photonic integration. This integration holds great potential for economical, energy-efficient, and foundry-scalable on-chip light sources, yet it has not been fully realized until now. In 2023, Wei et al. proposed a novel approach for the monolithic integration of embedded III-V lasers on silicon-on-insulator (SOI) substrates, as shown in Fig. 5(b). They demonstrated a maximum output power of 6.8 mW measured from the end tip of the butt-coupled silicon waveguides, with an estimated coupling efficiency of approximately -6.7 dB. This epitaxial integration method offers scalability and cost-effectiveness, enabling on-chip light sources that can be directly coupled to silicon photonic components. This breakthrough paves the way for future high-density photonic integration[77].

5 Photodetectors and CMOS integration

Photodetectors are essential components for optical communications, optical interconnect systems, and SS-OCT systems. While InP and InGaAs photodetectors have been the traditional choice due to their superior performance, the high cost and the difficulty of integrating these materials with CMOS technology have led to the exploration of silicon-based optoelectronic devices. Germanium photodetectors, known for their excellent absorption properties in the C-band and minimal lattice mismatch with silicon, have emerged as a promising alternative for Si-based optoelectronic systems. In 2017, Zhou et al. demonstrated germanium photodetectors integrated with standard CMOS technology, improving bandwidth and reducing dark current by optimizing the absorption length. Their photodetectors, incorporating distributed Bragg reflectors (DBRs), as shown in Fig. 5(c), achieved a bandwidth of 31.7 GHz with a 5 μm-long device, and reduced dark current to 7 nA at 1550 nm, and a consistent responsivity of 0.72 A/W at the optimized DBR positions[78]. These developments have paved the way for cost-effective, high-performance photodetectors in integrated optical systems.

While hybrid integration of III-V microdevices with Si/CMOS circuits remains a viable alternative to monolithic integration, overcoming the challenges of achieving low-defect III-V epitaxial material growth on Si, as well as merging the technological processes of III-V optoelectronics with Si-microelectronics, is crucial. One promising approach involves utilizing lateral light output, as demonstrated in III-V microdisk (MD) lasers. Kryzhanovskaya et al. showcased a heterogeneous integrated transceiver that combined an InGaAs/GaAs quantum-well MD laser with a closely spaced photodetector (PD) on a silicon board, using Au-Au thermocompression bonding, as shown in Fig. 5(d)[79].

Further advancements in monolithic integration, demonstrated by Kim et al. in 2015, involved a single-chip photonic transceiver integrating vertical-illumination Ge-on-Si photodetectors and VCSELs-on-Si on the same bulk-silicon substrate, achieving data rates of 50 Gb/s and 20 Gb/s, respectively[80], as shown in Fig. 5(e). These innovations have paved the way for low-power chip-level optical interconnects capable of operating at high speeds and facilitating on-

chip OCT. The prototype achieved 20 Gb/s low-power optical interconnects for λ~850 nm between fabricated chips, marking a significant milestone for high-speed, energy-efficient optical communications at the chip level. In 2022, Kacmoli and Gmachl further advanced on-chip integrated optics by demonstrating a mid-infrared photonic system composed of a laser, bus waveguide, and photodetectors, all fabricated on a single conventional λ = 8 μm quantum cascade laser (QCL) wafer[81], as shown in Fig. 5(f). This work highlighted the potential of on-chip integrated optics and its implications for advancing on-chip OCT technologies, offering new possibilities for high-performance, compact photonic systems in biomedical and communication applications.

5.1 Packaging and testing

The design and fabrication of laser and photodetectors lay the foundation for on-chip OCT systems. However, transforming these discrete optoelectronic components into a stable, reliable, and commercially viable system demands precise packaging and rigorous system-level testing. A critical prerequisite for practical OCT systems is to achieve low-loss coupling between integrated photonic chips and optical fibers. To minimize coupling losses, integrated optics chips must be carefully designed to match the mode field diameter of the fibers. This often requires developing high-precision alignment techniques and specialized mode-matching devices. In 2025, Missinne et al. proposed a versatile microlens integration platform designed to address key packaging challenges in PICs, particularly enhancing coupling efficiency and enabling the hybrid integration of external optical components, which are difficult to integrate monolithically[82]. In the same year, Jung et al. proposed 3D out-of-plane couplers that offer a peak transmission of -0.41 dB and broadband performance with losses below 0.55 dB[83]. These couplers provide high performance and versatility, advancing photonic packaging toward the scalability of electronic chip integration.

Beyond fiber-chip coupling, high-density photonic circuits present additional challenges in electrical packaging, which connects photonic components to the necessary electrical control systems and amplifiers. This includes managing power delivery, thermal dissipation, and signal processing. Thermal management becomes particularly challenge in high-density systems, where increased component density leads to higher heat generation. The shrinking dimensions, increased structural complexity, and 3D stacking of silicon–based semiconductor devices are intensifying challenges in thermal dissipation[84]. Without effective thermal management, the optical performance of the system may degrade, such as wavelength shifts, reduced component efficiency, and long-term reliability. While solutions such as thermal vias, microchannel cooling, and high-thermal-conductivity materials offer pathways for efficient heat dissipation, they inherently add design complexity. This not only increases manufacturing costs but also extends production timelines. Additionally, thermal crosstalk between electrical and photonic components must be minimized to prevent thermal-induced perturbations to critical parameters (e.g., emission wavelength, detection sensitivity), which could undermine the system's diagnostic precision. Milanizadeh *et al.* proposed a thermal eigenmode decomposition method to mitigate the effects of thermal crosstalk in arbitrary PICs, where thermal crosstalk is induced by physical effects, such as mutual mechanical stress and electromagnetic coupling among RF lines[85]. When PICs and electronic integrated circuits (EICs) are deployed together, the system-level integration approach that fuses these two chip types into a unified functional device is termed photonic-electronic co-packaging. Based on the specific integration methodologies, co-packaging technologies are classified into monolithic, 2D, 2.5D, and 3D. Monolithic co-packaging integrates both PICs and EICs onto a single chip via advanced manufacturing processes. Sun et al. reported a monolithic electronic-photonic system integrating over 70 million transistors and 850 photonic components, enabling logic, memory, and interconnect functions, including a microprocessor that uses on-chip photonic devices for optical inter-chip communication[86]. Most monolithic co-packaged devices have been fabricated using SOI substrates. For 2D co-packaging, discrete PICs and EICs are integrated side-by-side integration on a common substrate (e.g., printed circuit board or ceramic interposer) in a planar arrangement[87]. Communication between the two chip types occurs via wire bonding or short interconnections, without vertical stacking. In a 2.5D co-packaging, an intermediate interposer (typically silicon or glass) acts as a bridge between the PICs and EICs, which are mounted in a planar layout on the interposer. This approach combines the simplicity of 2D integration with enhanced high-speed, low-loss signal transmission. However, it faces challenges, such as the need for different solder materials for chip-interposer and interposer-PCB connections, requiring a stable hierarchical soldering process to mitigate warpage caused by mismatches in thermal expansion coefficients in multilayer structures[88]. Glass interposers support cost-effective panel-level packaging but require additional thermal management due to low thermal conductivity. Incorporating interconnect technologies such as embedded multi-die interconnect bridges or silicon bridges can enhance interconnection density and efficiency. Overall, 2.5D co-packaging offers superior scalability and flexibility, facilitating the convenient assembly of diverse PIC and EIC chips. For 3D co-packaging, PICs and EICs (or multiple stacks of these chips) are vertically stacked to form a 3D structure[89]. Interconnections are realized via through-silicon vias (TSVs), micro-bumps, or other vertical interconnect technologies, maximizing integration density and minimizing signal path length for ultra-high-speed communication. Typically, EICs are stacked atop PICs, with electrical

connections established through bumps on the PIC's top surface, TSV, and redistribution layers, making the device's electrical performance dependent on the quality of the electrical interconnections. However, like other heterogeneous bonding methods, 3D co-packaging's multilayer structure faces challenges such as material property mismatches, which can lead to cracks, failures, warpage, and other issues.

Wafer testing ensures packaged integrated photonic systems meet design specifications at the wafer-level. Wafer-level testing is indispensable for enabling scalable and cost-effective integrated photonic systems, as it evaluates large arrays of devices prior to dicing. To evaluate parameters, such as insertion loss, polarization dependence, and wavelength tuning across numerous devices, wafer-level testing methods such as automated optical and electrical wafer-scale testing must be developed. Trappen et al. proposed optical probes integrated with 3D-printed freeform coupling elements, which are designed to fit into deep-etched dicing trenches on the wafer surface[90]. This innovative design marks a pivotal advancement toward highly reproducible wafer-level testing of edge-coupled PICs. For OCT systems, testing is critical to validate integrated performance and evaluate key metrics such as signal-to-noise ratio and resolution in practical imaging scenarios. Packaging and testing costs remain a major barrier to the commercialization of integrated photonic OCT systems. While the initial chip-level design and fabrication are important, packaging and testing can account for a significant portion of the overall manufacturing cost. Innovations in automated testing systems, low-cost packaging materials, and mass production techniques will be essential to make these systems affordable for widespread clinical use. Developing cost-effective packaging solutions that allow for easy integration with existing OCT systems is key to ensure that integrated photonic circuits can compete with traditional OCT systems, particularly in terms of cost and scalability.

6 Research progress of on-chip integrated OCT

Current commercial and research OCT endoscopic systems primarily rely on fiber optics or free-space optics. While fiber optics and fiber-based components have contributed to making OCT systems lightweight and compact, further advancements in miniaturization, cost-efficiency, mass production, mechanical robustness, and precise alignment could be achieved with integrated optics. Recent advancements have focused on integrating key OCT components, such as beam splitters (BS)[97–99], broadband directional couplers (DC)[123,124], waveguide reference arms[104], optical waveguide delay lines (WDLs)[92,93,121], Michelson interferometers (MI)[91,94,95], Mach-Zehnder interferometers (MZI)[96,100,107,113], arrayed waveguide gratings (AWG)[101,109–111,115,16], waveguide spectrometers[110], and photodetectors (PDs)[103,105], as summarized in Table 2.

Over the past two decades, significant progress has been made in on-chip OCT, with integrated optics technology playing a crucial role in the development of highly compact and portable systems. In 2000, Culemann et al. pioneered the parallel integration of eight Michelson interferometers on a small glass chip, enabling the miniaturization of TD-OCT systems for more compact and affordable devices[91]. In 2010, Balbás et al. developed a miniature thermo-optic (TO) delay line in silicon, achieving a scan range of 0.95 mm without observable resolution loss, demonstrating the potential for miniaturized OCT components[92]. In 2014, Choudhary et al. demonstrated the use of an electro-optic (EO) modulator for fast scanning optical delay lines in TD-OCT, suggesting promising possibilities for future endoscopic OCT applications in biomedicine[93]. In 2010 and 2011, Yurtsever et al. studied a Michelson interferometer integrated on a silicon-on-insulator (SOI) platform, with dimensions of 1500 μm × 50 μm. Their system exhibited an axial resolution of approximately 40 μm, lower than the theoretical expectation of 27 μm. The system sensitivity was around 25 dB, with a loss of 10 dB caused by end coupling[94,95]. Further improvements, such as the addition of a broadband (>100 nm) spot size converter with coupling losses under 2 dB, were suggested to bring the sensitivity to a level sufficient for tissue imaging.

In 2013, Nguyen et al. demonstrated an integrated-optics-based SS-OCT system on the TriPleX platform, with a footprint of 0.4 cm × 1.8 cm, and the measured sensitivity was -80 dB, primarily due to a total coupling loss of 5 dB and system losses[96]. The schematic of the on-chip waveguide layout and the experimental setup is shown in Fig. 6(a), which is compared to a home-built bulk optics SS-OCT system shown in Fig. 6(b). The system successfully scanned a tissue phantom and visualized scattering layers at different depths, illustrating the feasibility of compact integrated systems for OCT. In 2014, Yurtsever et al. introduced an ultra-compact Si-integrated photonic interferometer for SS-OCT, as shown in Fig. 6(c) and 6(d). A three-layer tissue phantom was used to image. This system had a footprint of just 0.75 mm × 5 mm, with a sensitivity of -62 dB and 115 μW power delivered to the sample. A three-layer tissue phantom was used for imaging, and the results were averaged over 100 B-scans. The system revealed some residual background signal due to internal reflections in the chip[97]. In 2017, Zhou et al. proposed a wide-field, high-speed space-division multiplexing OCT system using an integrated photonic device. Their system achieved an eightfold increase in imaging speed by using a 1 × 8 splitter based on Si waveguides, with a chip size of approximately 2.5 cm × 2.0 cm. The system demonstrated an axial resolution of 11 μm in air (8.3 μm in tissue) and a sensitivity of ~91 dB[98]. In 2019, Hainberger et al. introduced further advancements in integrated optics by incorporating inverted taper structures and broadband power splitters, as well as polarization beam splitters on the silicon nitride (SiN) waveguide platform,

Table 2 | State-of-the-art integrated optics-OCT.

Abbreviation	MIs – Michelson Interferometers; WL–Wavelength; WDL–Waveguide Delay line; DL–Delay Line; TO – Thermo-Optic; MZI–Mach Zehnder Interferometer; SNR– Signal-to-Noise Ratio; DC–Directional Coupler;					
OCT type	**Waveguide device**	**Waveguide platform and size(μm)**	**WL (nm)**	**Date**	**Main features**	**Key challenges /Limitations**
TD-OCT	MIs	Silica waveguides	1300	2000[91]	Parallel integration of 8 MIs	Limited imaging speed
	WDL	SOI 3.0×few	1300	2010[92]	Integrated 10 kHz TO DL (driving voltage 40 V)	Limited A-line speed; No 3D imaging demonstration
	WDL	SiN	\	2014[93]	MOEMS optical delay line	No imaging demonstration.
SS-OCT	MI	SOI	1550	2010[94] 2011[95]	9 mm reference arm with reflector; Sensitivity 25 dB; Δz = 40 μm	Limited sensitivity and axial resolution; Sidewall roughness in silicon waveguides causing backscattering and signal loss
	MZI	TriPleX SiN strip 0.05×3.4	1300	2012[96]	Sensitivity 80 dB; lateral resolution 21 μm; Δz = 13 μm	Limited resolution
	Broadband BS	SOI rib 0.22×0.47	1300	2014[97]	Footprint of the interferometer only 0.75 mm × 5 mm; Sensitivity of 62 dB with 115 μW power delivered to the sample; Δz = 24.4 μm	Limited sensitivity
	1×8 BS	SOI	1310	2017[98]	Overall chip size:~2.5 cm × 2.0 cm; wide-field (up to 18.0 mm × 14.3 mm); 800k A-scans/s; Δz= ~ 8.3 μm in tissue, sensitivity ~91 dB	Imaging depth range
	Inverted taper, broadband BS, PBS	SiN	850	2019[99]	Propagation losses of 0.7 and 0.4 dB/cm for quasi-TE and quasi-TM polarizations, respectively.	Photonic building blocks, not yet applied in OCT systems.
	MZI	TriPleX SiN strip 0.05×3.4	1550	2018[100]	Sensitivity 83 dB with 40 μW back from sample arm. Δz = 15.2 μm in air	Better sensitivity by optimizing the design and fabrication methods
	Ge on Si integrated PDs	SOI	1550	2015[103]	Dual polarization, dual balanced, in-phase and quadrature detection	Compromised functionality and sensitivity; extending the center working wavelength to 1300 nm and 1060nm
	Reference arm On-chip micro-ball lens	SiON	1312	2016[104]	SNR = 71 dB with 2.6 mW of power on a mirror sample	Compromised sensitivity due to exclusion of a balanced detector
	MI, Ge integrated PD	SOI 220 nm thick	1300	2016[105]	Two versions with either internal (Sensitivity 53 dB) or external (Sensitivity 64 dB) reference path	Better sensitivities may be achieved based on technological and design improvements
	MZI, balanced diode pair	SiO_2	1310	2018[106]	Sensitivity 90 dB with 550 μW power on the sample	Limited imaging area (1.3 mm × 1.3 mm)
SD-OCT	AWG	SiON strip 0.8×2.0	1300	2011[109]	Integrated AWG (195 channels). External MI SNR: 75 dB. Δz = 19 μm in air	Sensitivity may be improved by fiber-to-chip coupling; limited channel number and imaging depth (1 mm)
	AWG	SiON strip 0.8×1.5/0.8×2.0	800/ 1300	2012[101]	AWG for 800 nm (125 channels): Δz=25 μm in air ;AWG for 1300 nm (195 channels): Δz=20 μm in air	1 mm imaging depth; Sensitivity limited by insertion losses; Still needs free-space MI + camera
	Spectrometer: AWG; BS	SiON 2.2×1.0	1300	2013[110]	SNR: 74 dB at 0.5 mW optical power on the sample; insertion loss:12 dB; Δz = 7.5 μm in tissue	Limited SNR and in-tissue depth ~1.4 mm
	AWG	SiON 1.0×1.8	1300	2013[111]	SNR = 74 dB. Δz = 7.5 μm	Limited SNR and in-tissue depth ~1.4 mm
	PCG	SiN	860	2014[112]	Δz = 9.6 μm in air; imaging depth of 2 mm in tissue;	External optical interferometer
	MZI	TriPleX SiN box-shaped 1.0×1.0	1300	2014[113]	External spectrometer; Sensitivity 65 dB; Δz =7.5 μm (SW dispersion comp.)	Requires external spectrometer; Low sensitivity
	Cascaded AWG	TriPleX SiN 75 nm thick	850	2019[114]	The cascaded AWG (512 channels) is directly attached to a CCD detector; Sensitivity ~77 dB; Δz = 5.9±0.4 μm in air	Imaging depth fundamentally limited by channel counts; low sensitivity
	AWG	SiN	850	2021[16]	Integrated AWG1 (256 channels): bandwidth 22 nm, sensitivity 91 dB (830 μW) and Δz = 10.7 μm in tissue; AWG2 (256 channels): bandwidth 48 nm, sensitivity 90 dB (480 μW) and Δz=6.5 μm in tissue	Requires external interferometer & camera; Packaging/alignment strongly impacts sensitivity; Partial integration
	Tunable DL	SiN	1300	2019[121]	Δz=6.5 μm in air; sensitivity 104 dB; On-chip DL extended the high-SNR imaging range by 0.6 mm	Limited A-line rate (28 kHz)
	Broadband BS	SiN	850	2019[122]	A wide bandwidth of 100 nm at various splitting ratios for TE, TM, and splitting ratios of 0.9/0.1, 0.8/0.2, 0.7/0.3, 0.6/0.4, and 0.5/0.5	Reported as simulation results
	Broadband DC based on tandem MZI, AWG	SOI	1310	2021[123]	The proposed DC with ~200 nm bandwidth	Careful co-design with AWG required
	BS based on SWG	SiN	850	2021[124]	110 nm bandwidth of the SWG-assisted DC was	Risk of exciting unwanted supermodes;

improving system performance[99]. Similarly, van Leeuwen et al. presented and characterized a Mach-Zehnder interferometer (MZI) using a SiN material platform, achieving high sensitivity (83 dB), an axial resolution of 15.2 μm in air, and a depth range of 2.5 mm[100]. Their work emphasized the advantages of SS-OCT, including simple single-element detection, improved sensitivity, and better imaging depth, despite some challenges with axial resolution and phase instability[101]. In 2020, Nevlacsil et al. demonstrated a polarization beam splitter (PBS) and a λ/4 path-separation scheme on a mature plasma-enhanced chemical vapor deposition SiN platform to reduce on-chip coupling loss. Based on this concept, an 840 nm SS-OCT PIC was developed, which demonstrated in- vivo retinal imaging and highlighted the CMOS compatibility of the platform. It clearly identifies the subsequent milestone as the monolithic co-integration of the photonic circuit with electronics on a single chip[102].

These studies contribute to the advancement of integrated optics and single-element detection. In 2015, Fujimoto et al. first proposed a silicon (Si) photonic integrated circuit SS-OCT receiver featuring dual-polarization, dual-balanced, in-phase, and quadrature (IQ) detection[103]. This integrated coherent receiver provided a miniaturized, cost-effective solution for SS-OCT and represented a key step toward the development of a fully integrated, high-speed SS-OCT system with multifunctional capabilities. In 2016, Chang et al. introduced an integrated optical probe incorporating an on-chip microlens within a common-path SS-OCT system[104]. The end facet of the silicon oxynitride (SiON)

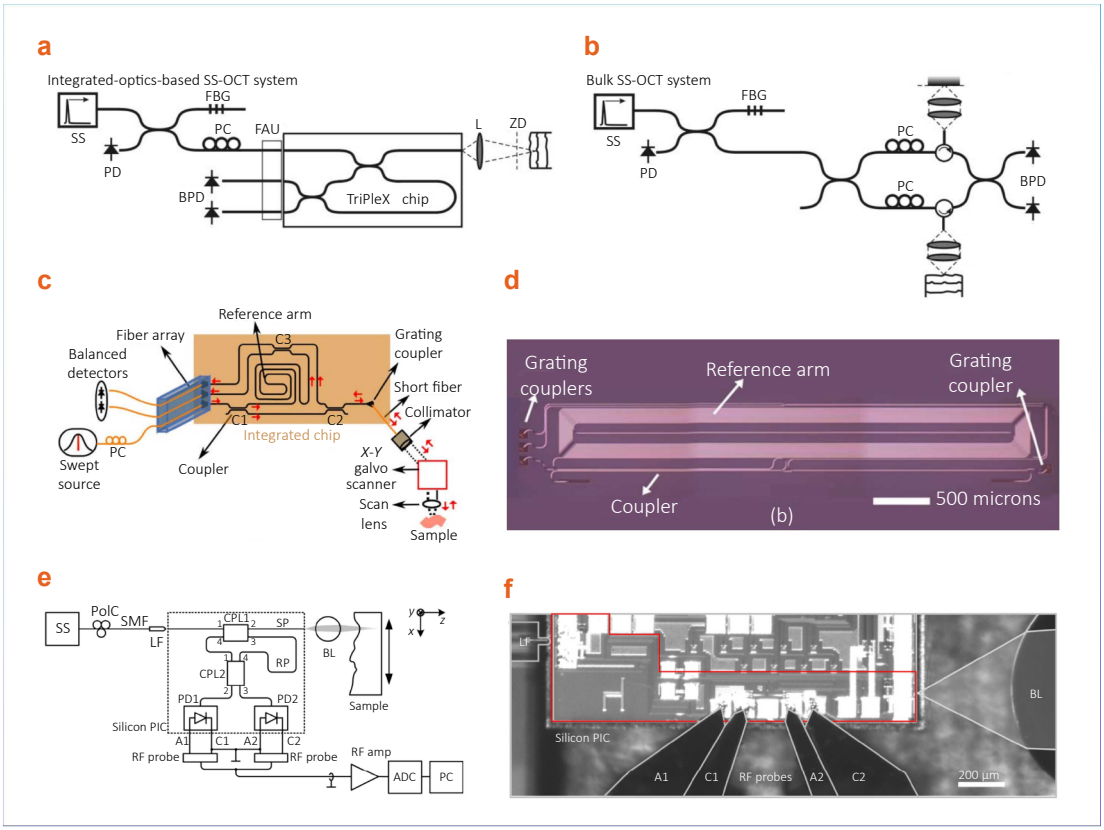

Fig. 6 | Schematic of the SS-OCT system based on integrated optics, including the reference arm[96,97], and PD[105]. (a,b) The experimental setup used for (a) the integrated-optics-based SS-OCT and (b) the bulk SS-OCT system. Reproduced with permission.[96]Copyright 2012, The Optical Society. SS, swept source; FBG, fiber Bragg grating; FAU, fiber array unit; PC, polarization controller; BPD, balanced photo detector; L, lens; PD, photodiode; and ZD, zero delay. (c) Schematic of the SS-OCT setup with the photonic integrated circuit. Reproduced with permission.[97]Copyright 2014, The Optical Society. C1, C2, C3: 2×2 couplers. The direction of the light was indicated by red arrows. (d) Microscope image of the fabricated photonic integrated interferometer. Reproduced with permission.[97]Copyright 2014, The Optical Society. (e) and (f) OCT system configuration with integrated reference path. (e) Schematic of setup. PolC, polarization controller; LF, lensed fiber; CPL1,2, 3 dB couplers; BL, ball lens; SP, sample path; RP, reference path; PD1,2, photodiodes with anodes (A1,2) and cathodes (C1,2); RF amp: RF amplifier; ADC, analog-to-digital converter; PC, personal computer. The photodiodes were contacted with RF probes, and their photocurrents were subtracted for balanced detection. (f) PIC microscope image with optical input (LF), optical port with free-space path (via BL) to and from the sample, along with electrical connections (via RF probes). The OCT system was co-integrated with a large number of additional optical circuits used for other purposes- the occupied on-chip area was indicated by a red frame and amounts to less than 0.4 mm^2. Reproduced with permission.[105]Copyright 2016, The Optical Society.

waveguide functioned as the reference plane in the common-path reference arm. The on-chip micro-ball lens enhanced the signal by up to 37 dB compared to a chip without a lens. The system achieved a signal-to-noise ratio (SNR) of 71 dB with an optical power of 2.6 mW when imaging a mirror sample.

That same year, Schneider et al. proposed two different SS-OCT implementations integrated on a silicon-on-insulator (SOI) photonic chip. One design featured an integrated reference path for imaging objects positioned 5 mm–10 mm from the chip edge, while the other utilized an external reference path compatible with conventional scanning heads. The OCT system incorporating an integrated reference path, integrated photodiodes, and an external swept-frequency source is shown in Fig. 6(e). In the sample path, a 1 mm diameter silica ball lens (BL) was employed to focus radiation from the chip facet and collect backscattered light from the sample. Fig. 6(f) presents a micrograph of the photonic integrated circuits, alongside the lensed fiber, ball lens, and radio frequency probe used to extract electrical signals from the photodiodes. To evaluate the system's imaging capabilities, 2D measurements were performed on a pumice sample. The porous surface structure was clearly visible; however, strong scattering limited measurable reflections from deeper regions within the material. Their proof-of-concept experiments demonstrated a sensitivity of -64 dB for OCT with an external reference path of variable length (OCT*ext*) and -53 dB for OCT with a fixed internal integrated reference path (OCT*int*), along with a dynamic range of 60 dB for OCT*ext* and 53 dB for OCT*int*[105].

Further advancements in SS-OCT systems followed. In 2018, Eggleston et al. introduced a chip-scale SS-OCT system with a high sensitivity of 90 dB[106]. The system utilized an Axsun SS-OCT laser with a center wavelength of 1310 nm, a sweep bandwidth of 140 nm, and a repetition rate of 100 kHz. In the same year, Guviernau et al. reported the first fully integrated OCT engine based on integrated optics, designed for multimodal point-of-care skin diagnostics[107]. This system featured compact dimensions of only 80 mm × 27 mm × 14 mm, achieving a lateral resolution of ~11 μm in tissue, an axial scanning range of 2.8 mm, a high sensitivity of -93 dB, and a 12 mm lateral field of view.

Most recently, in 2022, Fujimoto et al. introduced a high-speed SS-OCT system operating at 325 kHz with a long axial range of 15.5 mm, an axial resolution of 12.2 μm, and deep penetration capabilities for structural and angiographic imaging of the anterior eye[108]. This latest development underscores significant progress in the field. Collectively, these advancements highlight the increasing potential of integrated optics and chip-based systems in enhancing OCT imaging technologies. In recent years, several miniaturized SD-OCT systems have been developed, leveraging photonic integrated circuit technology to achieve both compactness and high performance.

7 Miniaturized integrated spectrometers

AWGs have become ideal candidates for integrated SD-OCT systems due to their high spectral resolution and compactness. In 2011, Nguyen et al. proposed a silicon oxynitride (SiON)-based AWG for SD-OCT, featuring a compact footprint of 3.0 cm × 2.5 cm and sensitivity of 75 dB[109]. Operating at a center wavelength of 1300 nm with a free spectral range of 78 nm, the spectrometer demonstrated a measured sensitivity of 75 dB. This value accounted for a 10 dB fiber-to-chip coupling loss, a 4 dB AWG insertion loss, and additional losses from chip-to-camera coupling. Figure 7(a) illustrates the proposed AWG spectrometer. The corresponding OCT image of a three-layered scattering phantom, acquired using this spectrometer, is shown in Fig. 7(b), where the dashed line marks the maximum imaging depth. The system achieved an axial resolution of 19 μm in air and an imaging depth of 1 mm. Despite the limitations posed by the number of output waveguides and depth range, the integration of AWGs has significantly contributed to miniaturizing OCT systems while maintaining high spectral resolution. In 2012, Akca et al. demonstrated an SD-OCT system incorporating an integrated optical spectrometer, utilizing two AWGs: a 195-channel AWG centered at 1300 nm and a 125-channel AWG with 0.16 nm channel spacing centered at 800 nm[101]. Both AWGs were fabricated using silicon oxynitride waveguide technology. The system achieved a maximum imaging depth of 1 mm, with axial resolutions of 25 μm and 20 μm in air for the 800 nm and 1300 nm center wavelengths, respectively. The signal processing steps for SD-OCT included acquiring the interference spectrum, subtracting the reference-arm spectrum, resampling to k-space, and performing a Fourier transform. The reflectivity depth profile was obtained by applying a Fourier transformation to the digitized camera output[101]. However, specific design-related challenges, such as free spectral range (FSR) limitations, polarization dependency, and curved focal planes, restrict their performance in on-chip SD-OCT applications.

In 2013, Akca et al. proposed advanced AWG designs to address these limitations. They also demonstrated a partially integrated OCT system incorporating an AWG spectrometer with a 136 nm FSR, 0.21 nm wavelength resolution, and an integrated beam splitter for *in vivo* imaging of human skin. This system achieved an axial resolution of 7.5 μm and a depth range of 1.4 mm, as shown in Fig. 7(c). The feasibility of on-chip OCT technology was validated through in-vivo imaging of human skin above the proximal interphalangeal joint of the middle finger. To enhance imaging quality, a contact gel was used as an index-matching agent, significantly reducing surface reflectivity. Figure 7(d) illustrates the averaged en-face view and corresponding cross-sectional tomograms, demonstrating the effectiveness of this approach. The measured SNR near the zero delay—where the optical path lengths of both interferometer arms are equal—was 74 dB at 0.5 mW optical power on the sample.

This included losses of 5 dB from fiber-to-chip coupling, 7 dB from fabrication imperfections, and 7.5 dB from double-pass transmission through standard microscope objectives. The SNR could be further improved by minimizing optical losses[110,111].

In 2014, Nitkowski et al. from Tornado Spectral Systems developed a new chip-based spectrometer, the OCT Advanced Nanophotonic Engine, for SD-OCT systems[112]. Their commercial prototypes featured a central wavelength of 860 nm, a spectral bandwidth of 70 nm, and 2048 output channels capable of independently recording TE and TM modes at an 80 kHz line scan rate. The system achieved a maximum imaging depth of 2.0 mm and an axial resolution of 6.8 μm in tissue.

That same year, Yurtsever et al. introduced an integrated interferometer for SD-OCT. The photonic circuit consisted of four splitters and a 190 mm long reference arm within a compact 10 mm × 33 mm Si_3N_4 waveguide platform[113]. This system achieved a sensitivity of 65 dB, which could be improved by reducing optical losses.

In 2019, Ruis et al. developed a miniaturized SD-OCT system based on a 512-channel integrated optics spectrometer using cascaded AWGs. The output waveguides were directly attached to a CCD detector, and the AWG had a compact footprint of 2.0 cm × 2.7 cm. The system achieved an SNR of 77 dB and an axial resolution of 5.9 μm ± 0.4 μm[114]. The cascaded AWG design enhanced the number of output channels and improved wavelength resolution. Similarly, Seyringer et al. introduced a compact, high-resolution 256-channel SiN-based AWG spectrometer for on-chip OCT. This spectrometer had a footprint of 13 mm × 14 mm and a spectral resolution of 0.1 nm[115]. In the same year, they also demonstrated a size-optimized 160-channel, 50-GHz Si_3N_4-based AWG spectrometer[116].

In 2021, Rank et al. used AWGs to perform *in vivo* 3D human retinal imaging for the first time with chip-based OCT and OCT angiography (OCTA)[16], as shown in Fig. 7(e). AWG 1 exhibited a bandwidth of 22 nm, a sensitivity of 91 dB (830 μW), and an axial resolution of 10.7 μm, while AWG 2 provided a bandwidth of 48 nm, a sensitivity of 90 dB (480 μW), and an axial resolution of 6.5 μm. The in-vivo retinal measurements include OCT images acquired without averaging and with five-fold averaging. To benchmark the performance of AWG-based OCT systems, a commercial SD-OCT system, the Cirrus 4000 (Zeiss, Jena, Germany), was used to image the same eye. The commercial system operated at an A-scan rate of 27 kHz with an axial resolution of 5 μm. A comparison of tomograms acquired using AWG-based and commercial OCT systems, illustrated in Fig. 7(f), revealed that despite the reduced bandwidth of AWG 1 and AWG 2, the external limiting membrane in the fovea tomogram remained distinguishable, albeit with slightly reduced contrast compared to the commercial system. The steep sensitivity roll-off of the

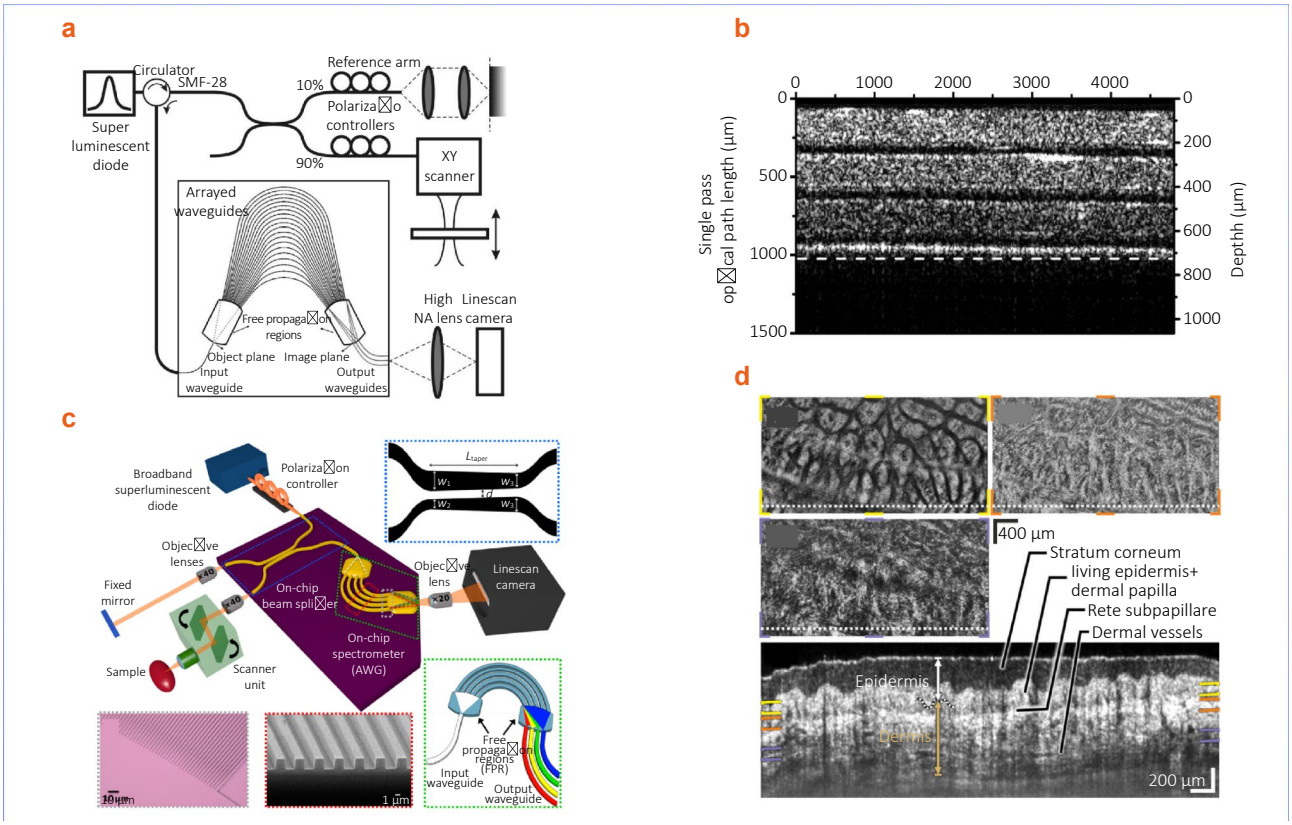

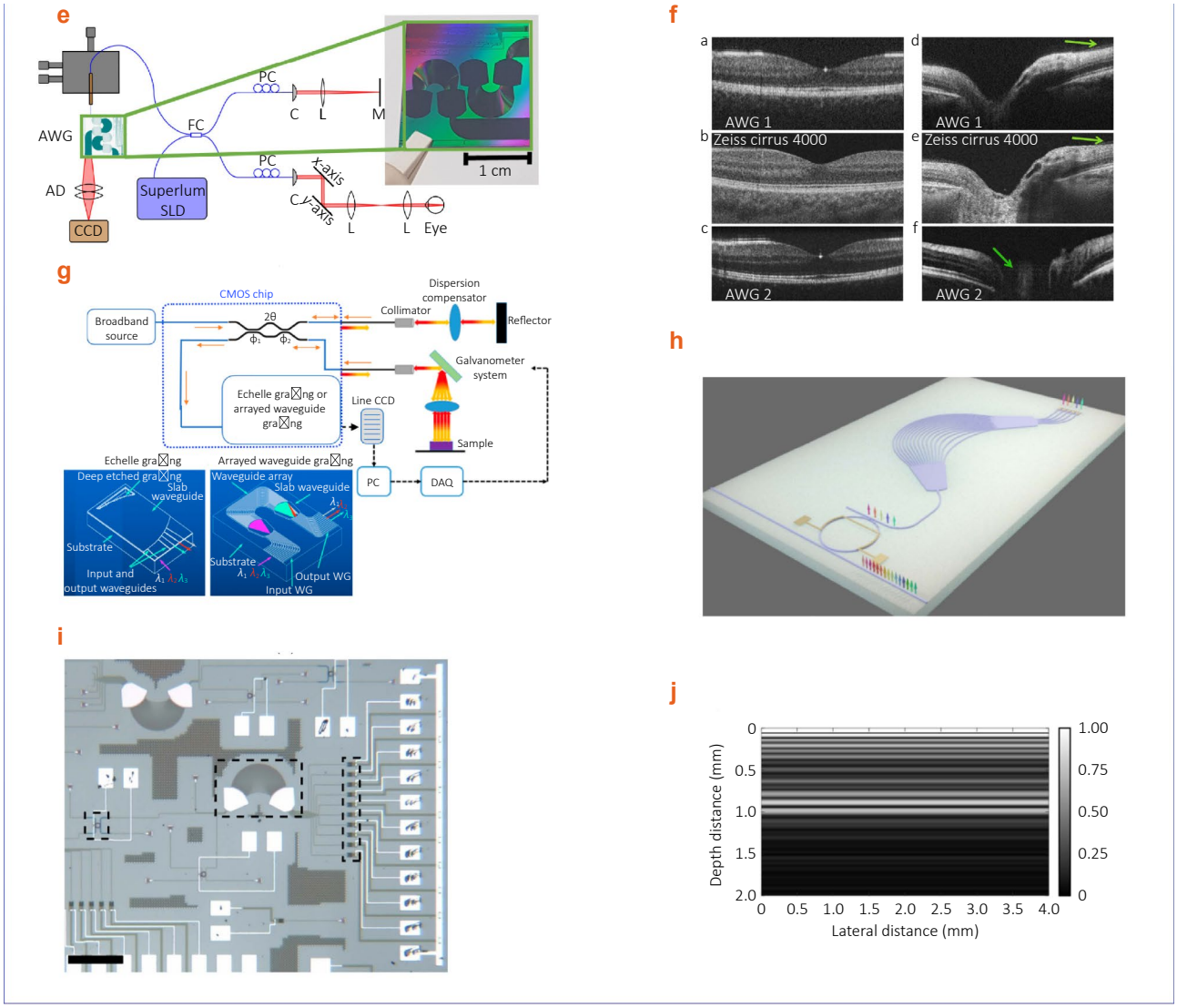

Fig. 7 | Schematic of SD-OCT system based on AWG or integrated spectrometer[16, 109, 111, 118–119]. (a) The experimental setup used for fiber-based SD-OCT with an AWG. Reproduced with permission.[109]Copyright 2011, The Optical Society. (b) OCT image of the three-layered scattering phantom measured with the AWG as a spectrometer in SD-OCT, the dashed line indicates maximum imaging depth. Reproduced with permission.[109]Copyright 2011, The Optical Society. (c) The partially integrated SD-OCT. Reproduced with permission.[111]Copyright 2013, The Optical Society. (d) Images of glabrous skin at the interdigital joint taken using the partially integrated SD-OCT system. Reproduced with permission.[111]Copyright 2013, The Optical Society. (e) Scheme of the SD-OCT on-chip setup. Reproduced under the terms of a CC-BY license.[16]Copyright 2021, The Authors. Published by Springer Nature. (f) OCT on a PIC system in comparison to a commercial OCT device. Direct comparison of the tomograms acquired with the SD-OCT on a PIC system with tomograms of the same eye acquired with a Zeiss Cirrus 4000. a, d Acquired with AWG 1 at 34kHz; b, e acquired with the Zeiss Cirrus 4000; c, f acquired with AWG 2 at 20kHz. The reduced imaging depth with AWG 2 can especially be observed, as the optic disc cup has poor contrast and an aliasing effect occurs (as indicated with green arrow) in f. The green arrows in d and e indicate the boundary of the vitreous. (g) Optical coupler-based SD-OCT interferometer. Reproduced with permission.[118]Copyright 2022, Published by MDPI. (h) Schematic of the integrated scanning spectrometer with tunable MRR and a single AWG. Direct electrical readout is enabled by on-chip germanium photodetectors. Reproduced with permission.[119]Copyright 2022, The Optical Society. (i) Microscope image of the integrated spectrometer with heater-controlled tunable MRR, 10-channel AWG, and integrated germanium photodetector array. Reproduced with permission.[119]Copyright 2022, The Optical Society. (j) B-frame obtained by scanning the sample across a straight line along the lateral direction. Reproduced with permission.[119]Copyright 2022, The Optical Society.

AWGs was evident in the diminished contrast of the choroid. Additionally, the limited overall imaging depth led to aliasing effects, as indicated by the green arrow in Fig. 7(f). These advancements highlight the growing clinical potential of miniaturized, chip-based OCT systems and demonstrate the feasibility of further integration and optimization for future applications.

A crucial component of on-chip OCT systems is the opti-

cal power splitter, which functions as an interferometer to combine the reflected signals from the reference and sample arms. In 2022, Zheng et al. proposed a chip-based SD-OCT system incorporating a Mach-Zehnder directional coupler and a spectrometer[118]. The spectrometer filtered the recombined signal and directed it into a line charge-coupled device (CCD) array, as illustrated in Fig. 7(g).

Given the need for integrated spectrometers with both high spectral resolution and wide optical bandwidths in SD-OCT, Zhang et al. developed a compact integrated scanning spectrometer using a tunable micro-ring resonator (MRR) combined with a single AWG, as shown in Fig. 7(h). This system operated with a channel spacing of 0.2 nm, providing a total of 350 wavelength channels and a scanning speed of 31 kHz within the 1265–1335 nm range[119]. Figure 7(i) presents a microscope image of the fully integrated spectrometer and germanium photodetectors fabricated on a multi-project wafer, with the AWG occupying a compact footprint of 270 μm × 200 μm.

To evaluate the performance of the OCT system utilizing this integrated scanning spectrometer, a multilayer dielectric-coated aluminum mirror on a borosilicate glass substrate was used as the sample. A galvo system scanned the light beam along a straight line, forming a B-frame. As shown in Fig. 7(j), the B-frame result revealed a strong reflection from the metal surface at a depth of approximately 1 mm. Furthermore, the axial resolution and overall image quality have the potential for further enhancement when all wavelength channels are utilized simultaneously.

In 2024, Agneter et al. demonstrated a CMOS-compatible, optoelectronic SD-OCT spectrometer that monolithically integrates a 512-channel AWG, photodiodes, multiplexers, analogue-to-digital converters, and control logic on a 2 cm × 2 cm PIC; the engine achieved ~70% waveguide-to-photodiode coupling efficiency and, in system tests, 92 dB sensitivity at 55 kHz with a 6 dB roll-off at 2 mm, enabling 3D in-vivo tomograms of zebrafish larvae and human skin[120]. This ground-breaking fully integrated spectrometer represents a significant step towards a miniaturized and cost-effective OCT system.

8 Optical power splitter and other optical devices

The on-chip tunable waveguide delay line and coupler play a pivotal role in on-chip OCT systems. In 2019, Ji et al. introduced an on-chip tunable photonic delay line for OCT[121]. As depicted in Fig. 8(a) and Fig. 8(b), this delay line is seamlessly integrated into a commercial SD-OCT system operating at a wavelength of approximately 1.3 μm. By replacing the system's reference arm, it effectively compensated for path length differences while maintaining a compact footprint, with the total chip size measuring just 8 mm^2. Utilizing ultralow-loss Si_3N_4 waveguides with integrated microheaters, the researchers extended the OCT imaging range by 0.6 mm while preserving a high signal-to-noise ratio (SNR). The axial resolution of the system, measured in air, was 6.5 μm. Figure 8(c) and Fig. 8(d) show OCT B-scans of the endocardium side of the tissue before and after tuning the delay line, respectively. Notably, after tuning, the SNR of both the surface area and deeper regions of the scan improved significantly. Furthermore, Fig. 8(e) and Fig. 8(f) compare onion images captured using the commercial SD-OCT system, with and without the tunable photonic delay line. These images clearly demonstrate that integrating the tunable delay line did not degrade image quality, ensuring undistorted visualization[121].

In the same year, Sharma et al. introduced a broadband beam splitter designed for OCT applications on a Si_3N_4 platform, depicted in Fig. 8(g). This splitter exhibited a broad spectral response over 100 nm, centered at 850 nm. Simulations of 50:50 broadband directional couplers (DCs) were conducted for both TE and TM modes at three different wavelengths[122]. Since commercial broadband light sources can operate over more than 150 nm—crucial for enhancing the axial resolution of OCT—optimizing broadband coupler designs to maximize wavelength flatness is essential.

In 2021, Widhianto et al. investigated the effect of optical power splitting on sensitivity and axial resolution in on-chip SD-OCT. They utilized a tandem Mach-Zehnder interferometer directional coupler (TMZDC) as a broadband coupler[123], as shown in Fig. 8(h). Simulations and experiments (Fig. 8(i)) revealed that the TMZDC device, designed with a 10:90 splitting ratio, achieved approximately 120 nm of spectral flatness centered at 1310 nm. To compensate for non-uniform AWG spectra and maintain sensitivity and axial resolution in on-chip SD-OCT, they proposed employing particle swarm optimization (PSO) to manipulate the Mach-Zehnder directional coupler (MZDC), resulting in a U-shaped wavelength compensation scheme.

Also in 2021, Dong et al. proposed a subwavelength grating (SWG)-assisted DC for beam splitting in 850 nm chip-based OCT applications[124]. As shown in Fig. 8(j), this beam splitter allowed for variable splitting ratios by simply adjusting the coupling region length (Fig. 8(k)). Notably, the unchanged axial point spread functions (PSFs) demonstrated that the splitting ratio did not affect OCT axial resolution. By carefully selecting SWG geometries—such as duty cycle and period—the bandwidth of the SWG-assisted DC was maximized to 110 nm, achieving an axial resolution better than 4 μm. Additionally, they showed that tuning the SWG period could effectively mitigate wavelength-mismatch-induced resolution degradation. The SWG-assisted DC also exhibited high fabrication tolerance, maintaining performance even in the presence of minor geometric variations.

These advancements highlight the potential for integrating high-performance spectrometers into compact, chip-based SD-OCT systems, paving the way for more efficient and portable OCT imaging technologies.

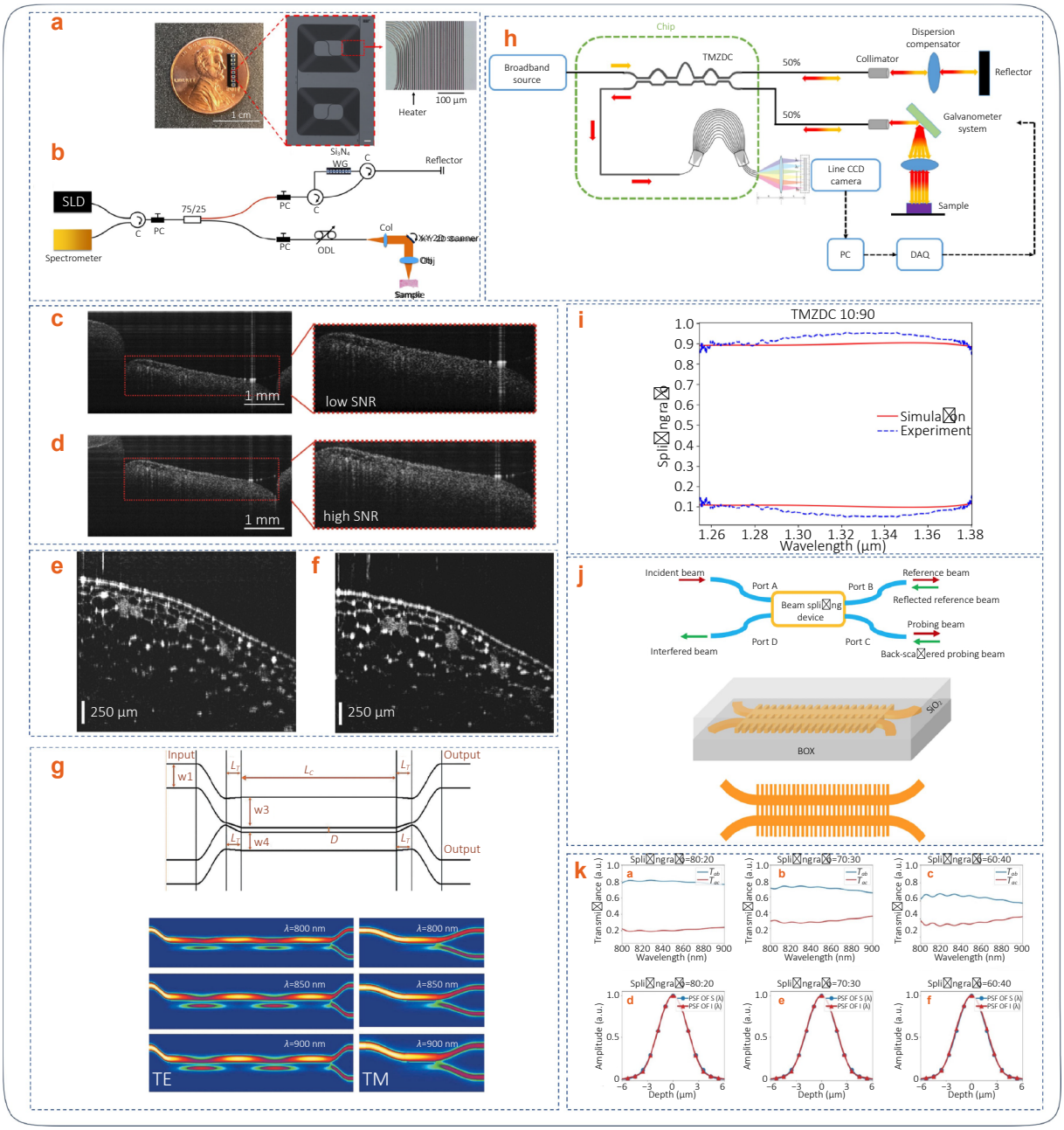

Fig. 8 | Schematic of SD-OCT system based on integrated optics, including tunable delay line[121], broadband DC[122- 124], AWG or integrated spectrometer[123]. (a) Fabricated 0.4 m long Si_3N_4 with an integrated platinum heater. (b) Schematic of the experimental setup for testing the tunable photonic delay line. C: circulator, PC: polarization controller, ODL: optical delay line, Col: collimation lens, WG: waveguide. Reproduced under the terms of a CC-BY license. Copyright 2019[122], Authors, AIP Publishing. (c) and (d) High-topology, high-SNR OCT imaging of a human right ventricle sample from the endocardium side, two images (c) and (d), taken before and after delay line tuning. Zoomed-in views were shown in the red box, and one can see that the SNR of the surface area with the lower part of the OCT scan was increased after the tuning. (e) and (f) Onion images taken with and without the tunable photonic delay line using the commercial SD OCT system. (e) Image taken with their chip tunable photonic delay line. (f) Image taken with the commercial system. (g) Broadband asymmetric DC and power distribution of the 50:50 broadband DCs for TE and TM modes at different wavelengths. Reproduced with permission.[122]Copyright 2019. Published by Taylor & Francis. (h) The configuration of the SD-OCT on-chip system, additional coupler before AWG input for flattening AWG output spectrum. Reproduced under the terms of a CC-BY license.[123]Copyright 2021. IEEE Photonics Society. (i) Simulation and experiment of tandem Mach-Zehnder DC 10:90. (j) Beam splitter for OCT and SWG-assisted DC. Reproduced under the terms of a CC-BY license.[124]Copyright 2021. IEEE Photonics Society. (k) Upper: Transmittance of the BS under splitting ratios of 80:20, 70:30, and 60:40. Lower: Axial PSFs obtained by DFT of the simulated light source S(λ) (blue dots) and the transmitted spectra I(λ) (red triangles) under splitting ratios of 80:20, 70:30, and 60:40. Reproduced under the terms of a CC-BY license.[124]Copyright 2021. IEEE Photonics Society.

The integration of optics in SD-OCT and SS-OCT systems has significantly contributed to reducing their overall size; however, it has not yet fully replaced all system components. While integrated optics has successfully substituted certain elements of OCT systems, its performance remains constrained by technological limitations. To date, no clinically deployed OCT system has achieved complete integration using solely on-chip optics, nor has any research system been composed entirely of integrated optics. This is primarily due to ongoing challenges in integrating both active and passive optical components onto a single chip. Nevertheless, the advancements in OCT technology leveraging integrated optics mark a significant step toward the ultimate goal of fully chip-based OCT systems.

9 OCT applications and integration with other modalities

All the integrated-optics device technologies described above can be used for both endoscopic and non-endoscopic OCT imaging systems. OCT has become an essential diagnostic tool in ophthalmology and cardiology and has also found successful applications in gastroenterology[3,126], gynecology[7], and urology[9] due to its high-resolution imaging capabilities[45, 129, 131]. In ophthalmology, OCT is widely used for quantitative retinal thickness assessment and qualitative evaluation of anatomical changes. Advances in OCT technology have expanded its clinical scope, enabling broader and deeper imaging with enhanced contrast, now capturing blood flow in addition to structural morphology[129]. In cardiology, OCT is increasingly utilized for intravascular imaging of coronary arteries, providing detailed visualization of plaque morphology and vessel wall characteristics[45, 131].

As technology advances, the clinical applications of OCT continue to expand, now encompassing preoperative, intraoperative[132], and postoperative imaging. This enables clinicians to diagnose diseases before treatment, monitor therapeutic interventions in real time, and assess the need for further treatment post-therapy.

Compared to traditional treatment modalities such as surgery, chemotherapy, and radiotherapy, PDT is a non-invasive or minimally invasive procedure that is highly selective. PDT targets specific cells or tissues, minimizing damage to surrounding healthy tissue.

The application of OCT in PDT is crucial due to its ability to provide detailed anatomical and vascular distribution information, ultimately enhancing therapeutic effects. OCT plays a key role in several stages: pre-treatment assessment, determination of the treatment area, real-time monitoring during treatment, and evaluation of therapeutic outcomes.

OCT's high resolution and limited imaging depth enable clear visualization of the microscopic structure of biological tissues. This helps accurately assess the location, extent, and depth of lesions, as well as the health of surrounding tissues. By ensuring PDT targets only the diseased tissue, OCT minimizes the potential for damage to healthy tissue.

Post-treatment, OCT can assess therapeutic outcomes, such as the regression of the lesion, helping clinicians adjust the treatment plan. This may include decisions on whether to repeat the treatment or modify the parameters for optimal results.

PDT has proven to be an effective treatment for choroidal neovascularization (CNV). In 2005, Krebs et al. demonstrated the use of OCT-guided retreatment for PDT, employing OCT measurements of retinal thickness to quantify PDT efficacy and assess the activity of neovascular lesions[133]. That same year, Alamán et al. utilized OCT to monitor PDT in patients with age-related macular degeneration (AMD). Their study included 53 patients (62 eyes) with AMD, and OCT helped visualize intraretinal or subretinal fluid, as well as the thickness of macular and choroidal neovascular complexes. This approach proved to be a useful complementary tool in determining the need for PDT and its potential reapplication in AMD patients[134].

In 2006, Layana et al. further demonstrated OCT's utility in assessing CNV activity before and after PDT in patients with pathological myopia. Their study included 33 patients (33 eyes) with pathological myopia who underwent PDT. Prior to treatment, OCT showed a high sensitivity of 96.77% for detecting CNV activity in AMD and 96.96% in pathological myopia. Post-treatment, OCT maintained strong sensitivity (95.65% for AMD and 95.23% for myopia), but moderate specificity (59.01% for AMD and 69.69% for myopia), resulting in diagnostic efficiencies of 82.95% and 79.62%, respectively[134,135].

These findings highlight OCT's role as an effective tool in assessing CNV activity, making it valuable for determining the necessity of PDT and guiding retreatment decisions in both AMD and pathological myopia patients.

PDT offers significant potential as a modern cancer treatment with minimal toxicity to normal tissue. In 2017, Sirotkina et al. proposed a vascular-targeting PDT using Chlorine E6, demonstrating that OCTA could precisely detect microvascular changes induced by PDT in a mouse ear tumor model (CT26)[136]. The OCTA images, captured before treatment, immediately after, 6 hours post-treatment, and a day later, revealed dynamic alterations in the microvascular network (Fig. 9(a-e)). Notably, the disappearance of microvascular structures post-PDT indicated thrombosis, blood vessel stasis, and disrupted blood flow, all of which contributed to the success of vascular-targeted PDT. The sensitivity of OCTA in detecting and quantifying these microvascular changes makes it an invaluable tool for monitoring PDT efficacy. By observing the microvessels surrounding the tumor, OCTA can potentially predict tumor necrosis and volume reduction.

However, the situation is more complex. While good microvascular response may be observed within tumor regions, the "normal" feeding vessels outside the tumor may

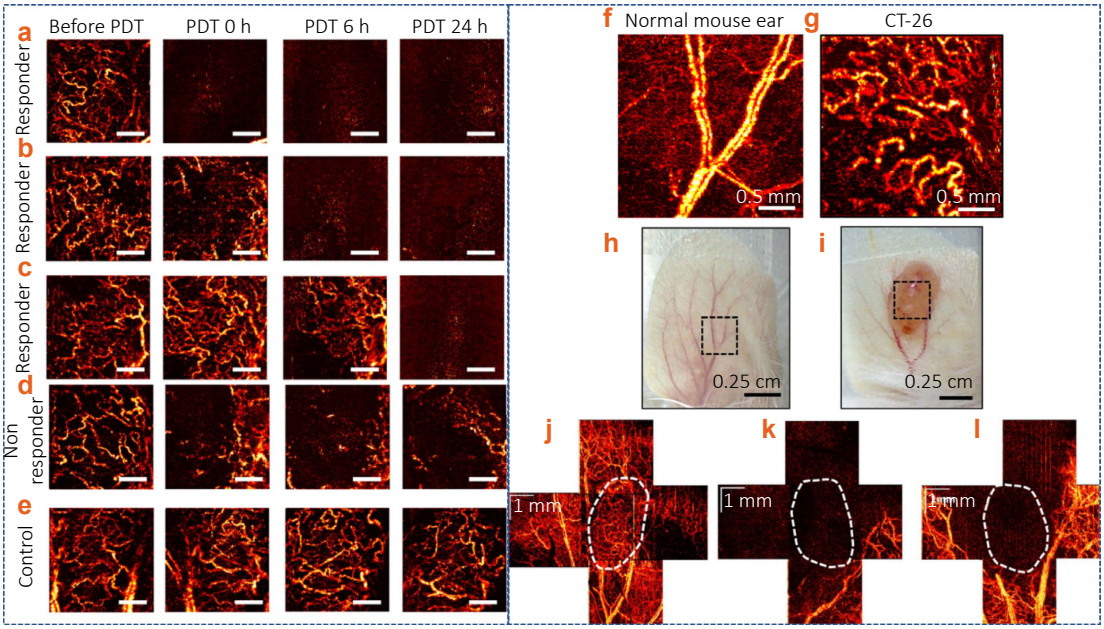

Fig. 9 | (a-e) OCTA images of microvascular alteration dynamics prior to, immediately following, 6 hours post, and a day after PDT (100 J/cm², 100 mW/cm²). Reproduced under the terms of a CC-BY license.[136]Copyright 2017, The Authors. Published by Springer Nature. A maximum intensity projection 2D display was shown for ease of comparison, representing a 3D data to depth of ~1.3 mm. (a-c) Three separate examples of responding tumors, showing significant microvascular alterations within a day of treatment (or less); (d) Example of a mildly responding tumor; (e) No microvascular changes were noted in the control animals; (f-i) Perfused microvascular network architecture in a mouse ear visualized by OCTA. Reproduced under the terms of a CC-BY license.[137]Copyright 2019, The Authors. Published by Springer Nature. (f) A 2D projection of 3D OCTA data showing typical normal ear microcirculation; (g) OCTA image of a CT-26 tumor growing in a mouse ear (two weeks after tumor cell inoculation). (h,i) were the white-light photograph counterparts of (f) and (g), respectively, showing the corresponding areas of the mouse ear. (j-l) OCTA images of tumor and peri-tumor perfused microvascular reaction at t=24 hours post PDT. Reproduced under the terms of a CC-BY license.[137]Copyright 2019, The Authors. Published by Springer Nature. (j) before PDT; (k) OCTA example of a responder (no visible perfused vessels in the tumor, and extremely low PVD in peri-tumor tissue). (l) OCTA example of a non-responder (no perfused vessels inside the tumor, but many perfused vessels in peri-tumor tissue). The tumor borders (indicated by dashed contours) were automatically segmented using a machine learning pixel classification technique.

remain unaffected, potentially leading to recirculation in previously treated areas. This complexity helps explain why tumors may shrink initially but later regrow, especially in moderate responders. Therefore, considering the role of surrounding "healthy" feeder vessels in determining long-term outcomes, increasing the PDT irradiation spot size to target these vessels could be a viable strategy to enhance treatment efficacy.

In 2019, Sirotkina et al. used OCTA as a minimally invasive, label-free, real-time bioimaging technique to visualize both healthy and pathological blood vessels and assess the treatment response after vascular-targeted PDT[137]. Visual inspection of OCTA images revealed significant differences in vascular structures between normal and tumor tissues (Fig. 9(f-g)). Due to active neovascularization and angiogenesis, tumor vasculature appeared denser and more tortuous compared to surrounding peri-tumor tissues. Fig. 9(h) and Fig. 9(i) display corresponding white-light photographs of the mouse ear, matching the areas shown in Fig. 9(f,g), respectively.

Before PDT, Fig. 9(j) shows OCTA imaging of perfused microvasculature in both tumor and peri-tumor regions. Post-treatment, 24 hours later, OCTA detected significant vascular reactions in both the tumor and peri-tumor tissue vessels (Fig. 9(k)). The absence of perfused vessels in the tumor, coupled with very low perfused vessel density (PVD) in the peri-tumor tissue, suggests successful PDT treatment in responders. However, in cases where no perfused vessels were detected in the tumor but some viable perfused vessels were present in the peri-tumor tissue (Fig. 9(l)), these animals were subsequently classified as non-responders to the treatment.

The assessment of microvascular networks within human basal cell carcinomas (BCC) and the surrounding skin tissue has been significantly enhanced through the combined use of OCTA and PDT. In 2019, Gubarkova et al. introduced OCTA for pre-treatment assessment and monitoring of treatment response following PDT in patients with BCC[138]. Their study, based on the analysis of 31 lesions, demonstrated that pre-treatment OCTA could accurately differentiate between common BCC subtypes, including nodular, superficial, and nodular-with-necrotic-core BCC, achieving a diagnostic accuracy of 78%. Additionally, post-treatment OCTA images taken 24 hours after PDT were highly predictive of

the ultimate treatment outcome, with a predictive accuracy of 98%[138].

In 2021, Hamdoon et al. further advanced this technology by proposing the use of in vivo OCTA-guided PDT for skin pre-cancer and cancer lesions. Their investigation revealed distinct microstructural variations between normal skin, pre-cancer tissue, and the transitional zone between these two types of tissue in OCT images[139]. By examining a cohort of 12 patients with 18 facial skin lesions before PDT, they were able to precisely map the tumor-free margins. This study not only demonstrated the technical viability of OCT in delineating real tumor boundaries but also monitored the skin alterations occurring post-PDT. This improved treatment efficacy and led to excellent cosmetic outcomes in 89% of patients. Furthermore, it established an optimized PDT efficacy model based on the correlation between the measured OCT features and the final treatment outcome[139]. The potential of this technology to personalize treatments is evident, optimizing outcomes while minimizing side effects. The future of skin cancer treatment is indeed looking brighter with OCTA offering real-time guidance.

Additionally, OCT can be combined with other imaging modalities, such as ultrasound (US) imaging and fluorescence imaging (FI), to enhance diagnostic capabilities.

For OCT and US dual-modality systems, Nie et al. (2021) evaluated the feasibility and effectiveness of a novel separable, ultrafine biliopancreatic duct endoscopy device integrating both US and OCT for in vivo assessment of the biliopancreatic duct system[140]. This endoscopy device enables simultaneous OCT and US scans, improving diagnostic precision. In 2022, Gong et al. introduced a custom-built intrauterine dual-modality (OCT/US) endoscopic imaging system, successfully achieving in vivo imaging of rabbit uteri for the first time[8]. The OCT/US system and probe are shown in Fig.10(a,b). In this setup, OCT provides detailed surface information of the endometrium, while US offers depth information of the uterus. The imaging procedure for a rabbit uterus in vivo is illustrated in Fig. 10(c).

For OCT and FI dual-modality systems, Pahlevaninezhad et al. (2016) reported a fiber optic-based endoscopic imaging system capable of combining Doppler OCT (DOCT) with autofluorescence imaging (AFI) for imaging peripheral airways[142]. Using a 0.9 mm diameter dual-clad fiber (DCF) catheter, they demonstrated endoscopic DOCT and AFI in small human airways in vivo to validate the system's performance. As shown in Fig. 10(d), the AFI excitation light was coupled into the core of the DCF, ensuring tightly focused excitation while efficiently collecting autofluorescence emission through the large-diameter inner cladding of the fiber.

Given the immense potential of OCT in various applications, it is crucial to consider both system cost and size. Current OCT endoscopy systems are not only bulky but also expensive, with dual-mode endoscope systems nearly matching the combined cost and size of two separate modalities. Additionally, integrating multiple imaging modes complicates the debugging process. However, integrated optics presents a promising solution. By reducing system size and cost while enhancing portability, integrated optics can make imaging systems more accessible to researchers and clinicians, ultimately accelerating the clinical adoption of OCT technology. While integrated optics is not yet widely implemented in OCT endoscopy or dual-modality imaging, ongoing research highlights its significant advantages. This suggests ample opportunities for the widespread adoption of integrated optics in future imaging systems.

10 The role of intelligent computational imaging in integrated OCT

Despite the considerable advantages of OCT, clinicians still face challenges related to complex image interpretation and inconsistent diagnostic accuracy. Besides, one major challenge is achieving high-quality, high-resolution imaging without reliance on costly, high-performance lasers and additional optical components. Integrating artificial intelligence (AI) and deep learning (DL) into OCT imaging represents a promising approach to overcoming these limitations. These techniques enable automated disease detection, real-time image processing, precise delineation of tumor margins, enhanced OCT image quality, improved diagnostic accuracy, and streamlined clinical workflows. Various DL models, such as convolutional neural networks (CNNs) and generative adversarial networks (GANs), have demonstrated significant potential in OCT imaging by excelling at critical tasks including image segmentation[143], artifact removal, noise reduction[144], and disease classification[145]. This integration significantly enhances OCT's clinical utility and diagnostic capability. In 2019, Devalla et al. introduced a customized deep learning framework designed specifically for denoising single-frame OCT B-scans. Their method significantly improved image quality metrics, notably increasing the signal-to-ratio (SNR) and contrast-to-noise ratio (CNR). Importantly, their approach also reduced scanning durations, thereby enhancing patient comfort and clinical practicality[140]. More recently, in 2023, Lee et al. proposed a novel framework leveraging raw interference fringes using deep neural networks. Their approach significantly enhanced axial and lateral resolution while effectively reducing speckle noise in OCT images. By directly utilizing raw data, this method demonstrated superior performance compared to traditional processing techniques, thus showcasing another pathway toward more accurate and efficient OCT imaging[141]. In 2024, Miladinović et al. conducted a comprehensive evaluation of deep learning architectures - including ResNet18/34/50, VGG16, and InceptionV3 for the classification of retinal pathologies versus healthy cases based on OCT images[145]. Their study specifically addressed two critical challenges in medical AI: data scarcity and label noise. The results demonstrated that all evaluated architec-

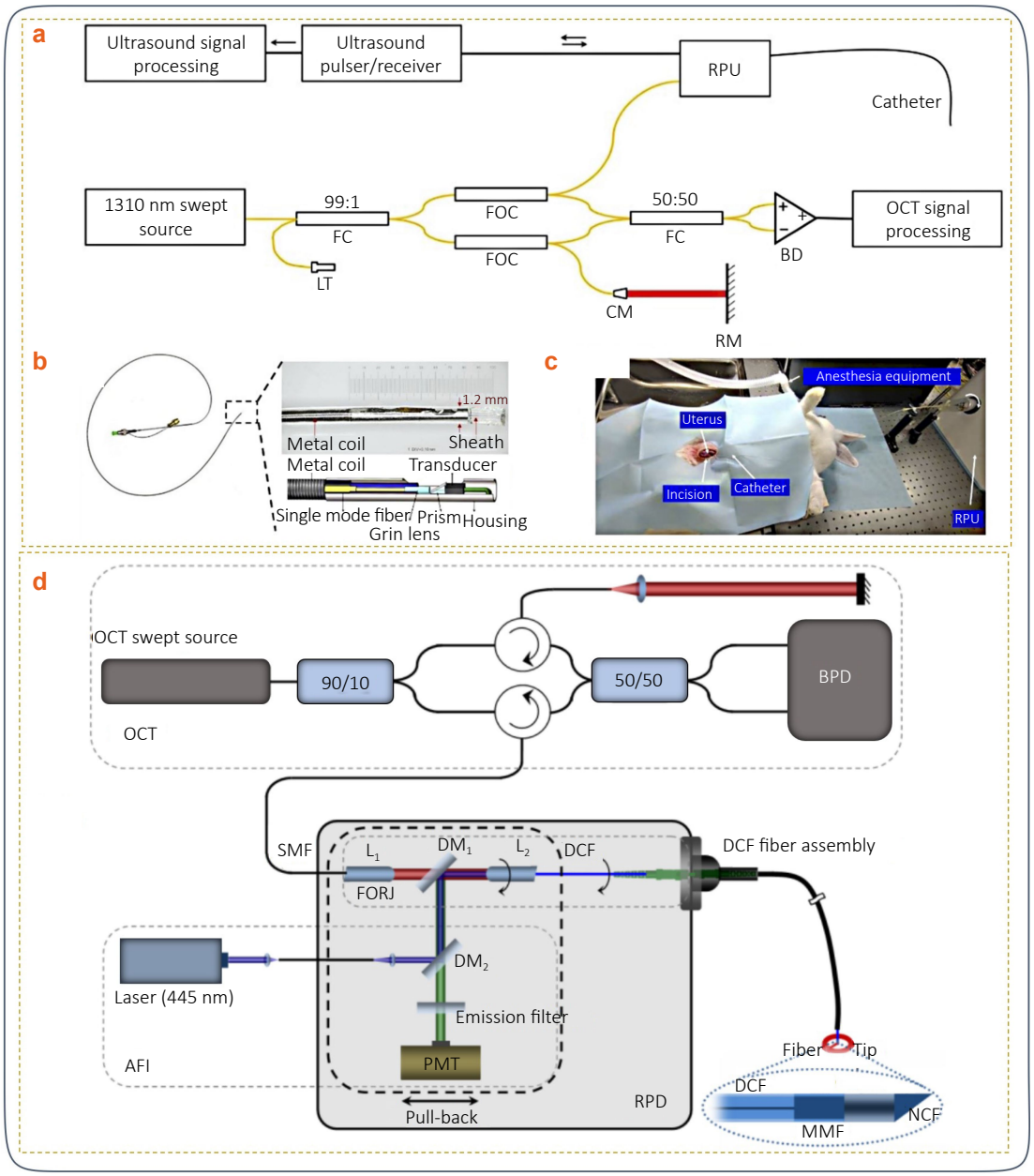

Fig. 10 | OCT-US and OCT-FI dual-modality endoscopic system and catheter[8,142]. (a) Schematic of the intrauterine dual-modality endoscopic system. Reproduced with permission.[8]Copyright 2022, The Optical Society. (b) The imaging catheter and its proximal sheath. Reproduced with permission.[8]Copyright 2022, The Optical Society. (c) Imaging procedure of a rabbit uterus in vivo. Reproduced with permission.[8]Copyright 2022, The Optical Society. RPU: rotational and pull-backing unit; FC: fiber coupler; LT: fiber-optic light trap; FOC: fiber optical circulator; CM: collimator; RM: reflective mirror; BD: balanced detector. (d) OCT-FI imaging system. L: Lens, DM: dichroic mirror; PMT: photomultiplier; FORJ: fiber optic rotary joint; RPD: rotary pull-back drive; NCF: no-core fiber; BPD: balanced photo-detector, Fiber Tip inset. Reproduced with permission.[142]Copyright 2015, The Optical Society.

tures achieved high classification accuracy (exceeding 90%) when trained on datasets containing 345 or more images. Notably, performance remained robust across different network architectures under these conditions, highlighting their potential for clinical applications despite limited data availability.

Besides, AI algorithms have shown immense promise in addressing the non-ideal behaviors of integrated optical components, such as thermal drift, channel crosstalk, and optical noise, all of which can degrade image quality and diagnostic accuracy. AI-powered solutions can mitigate these issues. For example, to address thermal drift, Seong et al. proposed a compact OCT system based on a single-board computer, employing software algorithms to compensate for thermal drift and eliminate the need for hardware modifications[142]. This system utilizes an area-scan

camera for real-time spectrometer monitoring and an automatic signal compensation algorithm that models temperature-induced distortion, computes corresponding parameters from real-time spectral data and inverts the distortion to restore image quality. Additionally, AI can assist in managing channel crosstalk in AWGs and micro-ring resonators, thereby ensuring more accurate spectrometer performance. For instance, Zhang et al. proposed an on-chip reconstructive spectrometer based on parallel cascaded micro-ring resonators integrated with AI for spectral reconstruction. By learning the nonlinear mapping between sampled intensity signals and the true incident spectrum, AI models help mitigate residual channel crosstalk, effectively separating overlapping spectral components and enabling accurate reconstruction of both continuous and sparse spectra within the 1450–1650 nm band[143]. Besides, You *et al.* proposed a CMOS-compatible miniaturized spectrometer integrated with self-referencing Fabry-Perot resonators and an AI reconstruction algorithm, which eliminates the need for manual algorithm parameter tuning while enabling wafer-scale production[144]. The device achieves a resolution of ~2.5 nm, an average wavelength deviation of ~0.27 nm, and a resolution-to-bandwidth ratio of ~0.46% within the 400–800 nm band, with the ability to resolve dual peaks separated by just 2.5 nm. This work not only paves the way for the commercialization of miniaturized spectrometers but also expands their potential in interdisciplinary fields such as medical diagnostics.

Furthermore, the quest for fully integrated, intelligent OCT systems aims to develop a chip-based OCT solution capable of autonomous operation, from photon generation to real-time AI-driven analysis. The integration of AI-powered on-chip computational imaging demands a comprehensive system where the entire imaging workflow —encompassing capture, processing, and diagnosis analysis—unfolds seamlessly on-chip, minimizing dependence on external components. In 2025, Liao *et al.* proposed and experimentally realized a NIR monolithic on-chip photonics system based on a perovskite/Si_3N_4 photonic platform[145]. They developed nano-hetero-integration technology to integrate efficient light-emitting diodes for photon generation, sensitive photodetectors for signal capture, and a 13-layer Si_3N_4 photonic neural network for on-chip computing. This system demonstrates the feasibility of unifying key photonic components and AI processing capabilities on a single chip with the neural network achieving over 85% test accuracy in edge detection task and 56% test accuracy on the CIFAR-10 image classification dataset. Moreover, the system exhibits low energy consumption (~100 fJ) and high computing speed (~2.2 Mbit s^{-1}), which can be optimized to up to ~2 Gbit s^{-1} by enhancing bandwidth. This work offers a promising solution for chip-integrated intelligent OCT systems by addressing the long-standing challenge of integrating diverse nanophotonic components onto a single chip, meeting the compactness and efficiency requirements of advanced integrated photonic systems.

11 Conclusion and future perspective

11.1 The future of integrated-optics OCT: advancements and clinical potential.

Integrated-optics OCT is an emerging technology currently in the research and development stage. Researchers are actively working to enhance on-chip OCT systems by improving imaging resolution, sensitivity, and speed. Additionally, various manufacturing methods and materials are being explored to create smaller, more cost-effective on-chip OCT systems. Notable progress has been made, including the development of high-performance on-chip arrayed waveguide gratings (AWG) for SD-OCT systems, as well as integrated splitters, MZI, and balanced photodiodes for SS-OCT systems. These advancements have already demonstrated promising imaging results in animal model experiments. The integration of compact light sources and detectors is paving the way for more efficient and portable OCT imaging technologies.

While integrated optics has significantly reduced the size of SD-OCT and SS-OCT systems, it currently replaces only certain components, which can impact overall system performance. To date, no clinically deployed OCT system has been built entirely with integrated optics, nor has any research system been composed solely of integrated optics. This limitation stems from ongoing challenges in integrating both active and passive optical components onto a single chip. The indirect bandgap of silicon makes it highly inefficient at emitting light, which is a significant challenge in integrating high-performance on-chip lasers. Current solutions focus on flip-chip/hybrid integration, heterogeneous integration, and direct epitaxial growth of III-V materials. Flip-chip/hybrid integration involves incorporating external light sources into silicon/Si_3N_4/LN waveguides via optical couplers. This approach allows individual devices to be fully tested and characterized before packaging, which enables the selection of high-performance chips and offers considerable design flexibility. It provides high flexibility, immediate yield, and the ability to select best-in-class lasers for coupling to Si/Si_3N_4 PICs, along with easy replacement and known long-term reliability. However, it faces limitations due to complex packaging requirements, reliance on III-V substrates, high manufacturing costs, a large footprint, and difficulties in achieving scalable on-chip laser integration. In contrast, heterogeneous integration involves direct bonding of III-V material substrates to silicon wafers using techniques such as low-temperature plasma bonding, followed by device processing. This approach addresses some of the low coupling efficiency and alignment challenges in earlier flip-chip methods. However, the continued dependence on III-V substrates in heterogeneous bonding schemes still

poses a barrier to significant cost reduction.

Direct epitaxial growth of III-V materials on silicon substrates is a promising pathway for large-wafer-scale, compactness, and high-volume manufacturing, potentially offering an ideal solution for the lack of integrated light sources in silicon photonics. However, this method is challenged by material incompatibilities such as difference in lattice constant, polar and non-polar mismatch, and disparities in thermal expansion coefficient between III/V compounds and silicon. These issues result in crystal defects, including antiphase domains, microcracks, and threading dislocations, which adversely affect device lifetime and performance. Furthermore, defect densities and wafer-scale uniformity continue to challenge yield and long-term reliability, including drift and aging. To mitigate these defects, some methods have been used, techniques such as asymmetric graded buffer layers and quantum-dot active regions have been employed to reduce threading dislocation density and improve temperature stability. OCT systems demands high output power (a few to tens of mW at the sample arm), long coherence length (narrow instantaneous linewidth), and a broad tuning range. Achieving broadband, fast, linear sweeps with narrow instantaneous linewidth is particularly challenging; integrating semiconductor optical amplifiers (SOAs) and wavelength selectors introduces additional design/thermal complexity. Moreover, the packaging and testing of PICs differ significantly from those of conventional electronic chips. Challenges in the field include high coupling loss, packaging warpage, difficult defect analysis, and a lack of standardized reliability verification methods. Despite these challenges, the development of integrated-optics OCT systems marks a critical step toward fully chip-based OCT solutions, with immense potential for further innovation and optimization in biomedical imaging.

11.2 Future prospects: Miniaturization, AI integration, and multimodal imaging.

Looking ahead, OCT endoscopy probes are expected to become smaller, allowing them to access narrow anatomical spaces. Future OCT systems will likely achieve higher spatial resolution, greater imaging depth, faster imaging speeds, and enhanced data processing capabilities. These improvements will enable high-throughput, real-time imaging for more precise in vivo clinical diagnoses. Additionally, the growing demand for OCT systems may drive advancements in cost-effectiveness, ease of manufacturing, and large-scale production—accelerating their widespread adoption in clinical practice. The development of portable, user-friendly OCT systems will further facilitate applications in outpatient diagnostics and remote healthcare.

In multimodal optical endoscopy, OCT is anticipated to be integrated with complementary imaging techniques such as fluorescence imaging and confocal microscopy. This combination will provide more comprehensive tissue structural and functional information, enhancing diagnostic accuracy. Additionally, integrated optical components such as AWGs and micro-ring resonators will contribute to the development of smaller, higher-performance OCT imaging devices.

Artificial intelligence (AI) is expected to play a pivotal role in on-chip OCT development, expanding its applications in image processing, feature recognition, and disease diagnosis. AI-driven techniques will facilitate the registration and fusion of multimodal images, improving the extraction of structural and functional details. This will enhance the accuracy and efficiency of clinical diagnoses, contributing to the advancement of personalized medicine. Ultimately, the convergence of on-chip OCT and AI technology will enable smarter, more efficient diagnostic and therapeutic solutions.

11.3 Clinical impact of on-chip OCT in medicine and biology.

On-chip OCT is poised to make a significant impact in medicine and biology by offering non-invasive, high-resolution, real-time imaging capabilities. In ophthalmology, it will aid in the diagnosis and monitoring of retinal disorders and glaucoma. In cardiology, it will provide high-definition imaging of coronary arteries, facilitating the assessment of vascular abnormalities.

OCT endoscopy is already being utilized across multiple medical specialties:

- **Gastroenterology:** Early detection of gastrointestinal diseases, assessment of mucosal abnormalities, and treatment monitoring.
- **Urology:** Precise imaging of the urinary tract and prostate, aiding in the diagnosis of conditions such as bladder cancer and benign prostatic hyperplasia.
- **Pulmonology:** Evaluation of lung tissue structure and diagnosis of respiratory disorders.
- **Gynecology:** Examination of cervical and uterine tissues, early detection of abnormalities, and guidance for biopsies.

Overall, on-chip OCT endoscopy provides valuable insights into the structural and pathological characteristics of biological tissues. Its continued development will enhance disease diagnosis, treatment planning, and real-time monitoring across various medical disciplines, reinforcing its role as atransformative imaging technology in modern healthcare.

References

1. Huang D, Swanson EA, Lin CP et al. Optical coherence tomography. *Science* **254**, 1178–1181 (1991).
2. Drexler W, Morgner U, Ghanta RK et al. Ultrahigh-resolution ophthalmic optical coherence tomography. *Nat Med* **7**, 502–507 (2001).
3. Bouma BE, Tearney GJ, Compton CC et al. High-resolution imaging of the human esophagus and stomach in vivo using optical

coherence tomography. *Gastrointest Endosc* **51**, 467–474 (2000).
4. Tearney GJ, Brezinski ME, Bouma BE et al. In vivo endoscopic optical biopsy with optical coherence tomography. *Science* **276**, 2037–2039 (1997).
5. Tearney GJ, Brezinski ME, Boppart SA et al. Catheter-based optical imaging of a human coronary artery. *Circulation* **94**, 3013 (1996).
6. Hanna N, Saltzman D, Mukai D et al. Two-dimensional and 3-dimensional optical coherence tomographic imaging of the airway, lung, and pleura. *J Thorac Cardiov Surg* **129**, 615–622 (2005).
7. Escobar PF, Belinson JL, White A et al. Diagnostic efficacy of optical coherence tomography in the management of preinvasive and invasive cancer of uterine cervix and vulva. *Int J Gynecol Cancer* **14**, 470–474 (2004).
8. Zhang JK, Du M, Fang JH et al. *In vivo* evaluation of endometrium through dual-modality intrauterine endoscopy. *Biomed Opt Express* **13**, 2554–2565 (2022).
9. Tearney GJ, Brezinski ME, Southern JF et al. Optical biopsy in human urologic tissue using optical coherence tomography. *J Urol* **157**, 1915–1919 (1997).
10. Fercher AF, Drexler W, Hitzenberger CK et al. Optical coherence tomography-principles and applications. *Rep Prog Phys* **66**, 239–303 (2003).
11. Zhang J, Chen ZP, Isenberg G. Gastrointestinal optical coherence tomography: clinical applications, limitations, and research priorities. *Gastrointest Endosc Clin N Am* **19**, 243–259 (2009).
12. Osiac E, Săftoiu A, Gheonea DI et al. Optical coherence tomography and Doppler optical coherence tomography in the gastrointestinal tract. *Word J Gastroenterol* **17**, 15–20 (2011).
13. Fujimoto JG, Brezinski ME, Tearney GJ et al. Optical biopsy and imaging using optical coherence tomography. *Nat Med* **1**, 970–972 (1995).
14. Sauk J, Coron E, Kava L et al. Interobserver agreement for the detection of Barrett's esophagus with optical frequency domain imaging. *Dig Dis Sci* **58**, 2261–2265 (2013).
15. Iftimia N, Park J, Maguluri G et al. Investigation of tissue cellularity at the tip of the core biopsy needle with optical coherence tomography. *Biomed Opt Express* **9**, 694–704 (2018).
16. Rank EA, Sentosa R, Harper DJ et al. Toward optical coherence tomography on a chip: in vivo three-dimensional human retinal imaging using photonic integrated circuit-based arrayed waveguide gratings. *Light Sci Appl* **10**, 6 (2021).
17. Shelton RL, Jung W, Sayegh SI et al. Optical coherence tomography for advanced screening in the primary care office. *J Biophotonics* **7**, 525–533 (2014).
18. Fercher AF, Hitzenberger CK, Kamp G et al. Measurement of intraocular distances by backscattering spectral interferometry. *Opt Commun* **117**, 43–48 (1995).
19. Yuan W, Brown R, Mitzner W et al. Super-achromatic monolithic microprobe for ultrahigh-resolution endoscopic optical coherence tomography at 800 nm. *Nat Commun* **8**, 1531 (2017).
20. Tsai TH, Potsaid B, Tao YK et al. Ultrahigh speed endoscopic optical coherence tomography using micromotor imaging catheter and VCSEL technology. *Biomed Opt Express* **4**, 1119–1132 (2013).
21. Feroldi F, Willemse J, Davidoiu V et al. *In vivo* multifunctional optical coherence tomography at the periphery of the lungs. *Biomed Opt Express* **10**, 3070–3091 (2019).
22. Fujimoto JG, Pitris C, Boppart SA et al. Optical coherence tomography: an emerging technology for biomedical imaging and optical biopsy. *Neoplasia* **2**, 9–25 (2000).
23. Kirtane TS, Wagh MS. Endoscopic Optical Coherence Tomography (OCT): advances in gastrointestinal imaging. *Gastroenterol Res Pract* **2014**, 376367 (2014).
24. Qin X, Wang BH, Boegner D et al. Indoor localization of hand-held OCT probe using visual odometry and real-time segmentation using deep learning. *IEEE Trans Biomed Eng* **69**, 1378–1385 (2022).
25. Fercher AF. Optical coherence tomography. *J Biomed Opt* **1**, 157–173 (1996).
26. Chinn SR, Swanson EA, Fujimoto JG. Optical coherence tomography using a frequency-tunable optical source. *Opt Lett* **22**, 340–342 (1997).
27. Wojtkowski M, Leitgeb R, Kowalczyk A et al. In vivo human retinal imaging by Fourier domain optical coherence tomography. *J Biomed Opt* **7**, 457–463 (2002).
28. Li GQ, Sun PC, Lin PC et al. Interference microscopy for three-dimensional imaging with wavelength-to-depth encoding. *Opt Lett* **25**, 1505–1507 (2000).
29. Golubovic B, Bouma BE, Tearney GJ et al. Optical frequency-domain reflectometry using rapid wavelength tuning of a Cr^{4+}: forsterite laser. *Opt Lett* **22**, 1704–1706 (1997).
30. Drexler W. Ultrahigh-resolution optical coherence tomography. *J Biomed Opt* **9**, 47–74 (2004).
31. Zhao TY, Mauger T, Li GQ. Optimization of wavefront-coded infinity-corrected microscope systems with extended depth of field. *Biomed Opt Express* **4**, 1464–1471 (2013).
32. Li ZZ, Fischer A, Li W et al. Volumetric retinal fluorescence microscopic imaging with extended depth of field. *Proc SPIE* **9713**, 97131C (2016).
33. Lan GP, Mauger TF, Li GQ. Design of high-performance adaptive objective lens with large optical depth scanning range for ultra-broad near infrared microscopic imaging. *Biomed Opt Express* **6**, 3362–3377 (2015).
34. Lan GP, Li GQ. Design of adaptive objective lens for ultrabroad near infrared imaging. *Proc SPIE* **9713**, 971314 (2016).
35. Pahlevaninezhad H, Khorasaninejad M, Huang YW et al. Nano-optic endoscope for high-resolution optical coherence tomography in vivo. *Nat Photon* **12**, 540–547 (2018).
36. Pahlevaninezhad M, Huang YW, Pahlevani M et al. Metasurface-based bijective illumination collection imaging provides high-resolution tomography in three dimensions. *Nat Photon* **16**, 203–211 (2022).
37. Lyu J, Ren L, Liu QY et al. Swept-source endoscopic optical coherence tomography real-time imaging system based on GPU acceleration for axial megahertz high-speed scanning. *Eur Rev Med Pharmacol Sci* **26**, 7349–7358 (2022).
38. Lan GP, Li GQ. Design of a *k*-space spectrometer for ultra-broad waveband spectral domain optical coherence tomography. *Sci Rep* **7**, 42353 (2017).
39. Gora MJ, Suter MJ, Tearney GJ et al. Endoscopic optical coherence tomography: technologies and clinical applications [Invited]. *Biomed Opt Express* **8**, 2405–2444 (2017).
40. Xi JF, Murari K, Zhang YY et al. OCT endomicroscopy and functional integration with two-photon fluorescence imaging. In *Bio-Optics: Design and Application 2011* BWA5 (Optica Publishing Group, 2011). https://doi.org/10.1364/BODA.2011.BWA5.
41. Xi JF, Huo L, Wu YC et al. High-resolution OCT balloon imaging catheter with astigmatism correction. *Opt Lett* **34**, 1943–1945 (2009).
42. Lee J, Chae Y, Ahn YC et al. Ultra-thin and flexible endoscopy probe for optical coherence tomography based on stepwise transitional core fiber. *Biomed Opt Express* **6**, 1782–1796 (2015).
43. Miao YS, Jing JC, Desai V et al. Automated 3D segmentation of methyl isocyanate-exposed rat trachea using an ultra-thin, fully fiber optic optical coherence endoscopic probe. *Sci Rep* **8**, 8713 (2018).
44. Li JW, Thiele S, Quirk BC et al. Ultrathin monolithic 3D printed optical coherence tomography endoscopy for preclinical and clinical use. *Light Sci Appl* **9**, 124 (2020).
45. Liu LB, Gardecki JA, Nadkarni SK et al. Imaging the subcellular structure of human coronary atherosclerosis using micro–optical coherence tomography. *Nat Med* **17**, 1010–1014 (2011).
46. Chu KK, Unglert C, Ford TN et al. *In vivo* imaging of airway cilia and mucus clearance with micro-optical coherence tomography. *Biomed Opt Express* **7**, 2494–2505 (2016).

47. Wijesundara K, Zdanski C, Kimbell J et al. Quantitative upper airway endoscopy with swept-source anatomical optical coherence tomography. *Biomed Opt Express* **5**, 788–799 (2014).
48. Liao WC, Chen TY, Wang CM et al. Endoscopic optical coherence tomography with a focus-adjustable probe. *Opt Lett* **42**, 4040–4043 (2017).
49. Delacrétaz Y, Boss D, Lang F et al. Endoscopic low coherence interferometry in upper airways. *Proc SPIE* **7372**, 73721Z (2009).
50. Mavadia-Shukla J, Liang WX, Mitzner W et al. *In vivo* airway imaging with high-speed ultrahigh-resolution endoscopic OCT. In *Optical Tomography and Spectroscopy 2016* OTu4C. 4 (Optica Publishing Group, 2016). https://doi.org/10.1364/OTS.2016.OTu4C.4.
51. Kohlfaerber T, Pieper M, Münter M et al. Dynamic microscopic optical coherence tomography to visualize the morphological and functional micro-anatomy of the airways. *Biomed Opt Express* **13**, 3211–3223 (2022).
52. Byun H, Kim YH, Xing JC et al. Utilization potential of intraluminal optical coherence tomography for the Eustachian tube. *Sci Rep* **11**, 6219 (2021).
53. Iyer JS, Yin BW, Stankovic KM et al. Endoscoscopy of the human cochlea using a micro-optical coherence tomography catheter. *Sci Rep* **11**, 17932 (2021).
54. Singh P, Chak A, Willis JE et al. In vivo optical coherence tomography imaging of the pancreatic and biliary ductal system. *Gastrointest Endosc* **62**, 970–974 (2005).
55. Westphal V, Rollins AM, Willis J et al. Correlation of endoscopic optical coherence tomography with histology in the lower-GI tract. *Gastrointest Endosc* **61**, 537–546 (2005).
56. Yuan W, Mavadia-Shukla J, Ngamruengphong S et al. Mo1994 ultrahigh resolution endoscopic optical coherence tomography at 800 nm for imaging of bile duct. *Gastrointest Endosc* **83**, AB487 (2016).
57. Yuan W, Feng Y, Chen DF et al. *In vivo* assessment of inflammatory bowel disease in rats with ultrahigh-resolution colonoscopic OCT. *Biomed Opt Express* **13**, 2091–2102 (2022).
58. Pfau PR, Sivak MV, Chak A et al. Criteria for the diagnosis of dysplasia by endoscopic optical coherence tomography. *Gastrointest Endosc* **58**, 196–202 (2003).
59. Tsai TH, Lee HC, Ahsen OO et al. Ultrahigh speed endoscopic optical coherence tomography for gastroenterology. *Biomed Opt Express* **5**, 4387–4404 (2014).
60. Jing JC, Chou L, Su E et al. Anatomically correct visualization of the human upper airway using a high-speed long range optical coherence tomography system with an integrated positioning sensor. *Sci Rep* **6**, 39443 (2016).
61. Adler DC, Zhou C, Tsai TH et al. Three-dimensional endomicroscopy of the human colon using optical coherence tomography. *Opt Express* **17**, 784–796 (2009).
62. Xi JF, Huo L, Li JS et al. Generic real-time uniform K-space sampling method for high-speed swept-source optical coherence tomography. *Opt Express* **18**, 9511–9517 (2010).
63. Liang KC, Ahsen OO, Wang Z et al. Endoscopic forward-viewing optical coherence tomography and angiography with MHz swept source. *Opt Lett* **42**, 3193–3196 (2017).
64. Liang KC, Wang Z, Ahsen OO et al. Cycloid scanning for wide field optical coherence tomography endomicroscopy and angiography *in vivo*. *Optica* **5**, 36–43 (2018). https://doi.org/10.1364/OPTICA.5.000036.
65. Mavadia-Shukla J, Fathi P, Liang WX et al. High-speed, ultrahigh-resolution distal scanning OCT endoscopy at 800 nm for *in vivo* imaging of colon tumorigenesis on murine models. *Biomed Opt Express* **9**, 3731–3739 (2018).
66. Park BH, Pierce MC, Cense B et al. Real-time multi-functional optical coherence tomography. *Opt Express* **11**, 782–793 (2003).
67. Adams DC, Suter MJ. Processing-based approach for resolving the sample optic axis in endoscopic polarization-sensitive optical coherence tomography. *Opt Express* **26**, 24917–24927 (2018).
68. Willemse J, Wener RR, Feroldi F et al. Polarization-sensitive optical coherence tomography in end-stage lung diseases: an ex vivo pilot study. *Biomed Opt Express* **12**, 6796–6813 (2021).
69. Adams DC, Majid A, Suter MJ. Polarization mode dispersion correction in endoscopic polarization-sensitive optical coherence tomography with incoherent polarization input states. *Biomed Opt Express* **13**, 3446–3460 (2022).
70. Tilma BW, Jiao YQ, Kotani J et al. Integrated tunable quantum-dot laser for optical coherence tomography in the 1.7 μm wavelength region. *IEEE J Quantum Electron* **48**, 87–98 (2012).
71. Chen SM, Li W, Wu J et al. Electrically pumped continuous-wave III–V quantum dot lasers on silicon. *Nat Photon* **10**, 307–311 (2016).
72. Shi YT, Wang ZC, Van Campenhout J et al. Optical pumped InGaAs/GaAs nano-ridge laser epitaxially grown on a standard 300-mm Si wafer. *Optica* **4**, 1468–1473 (2017).
73. Zhu S, Shi B, Li Q et al. Room-temperature electrically-pumped 1.5 μm InGaAs/InAlGaAs laser monolithically grown on on-axis (001) Si. *Opt Express* **26**, 14514–14523 (2018).
74. Hu YT, Liang D, Mukherjee K et al. III/V-on-Si MQW lasers by using a novel photonic integration method of regrowth on a bonding template. *Light Sci Appl* **8**, 93 (2019).
75. Haindl R, Duelk M, Gloor S et al. Ultra-high-resolution SD-OCM imaging with a compact polarization-aligned 840 nm broadband combined-SLED source. *Biomed Opt Express* **11**, 3395–3406 (2020).
76. Yan Z, Han Y, Lin LY et al. A monolithic InP/SOI platform for integrated photonics. *Light Sci Appl* **10**, 200 (2021).
77. Wei WQ, He A, Yang B et al. Monolithic integration of embedded III-V lasers on SOI. *Light Sci Appl* **12**, 84 (2023).
78. Cui JS, Zhou ZP. High-performance Ge-on-Si photodetector with optimized DBR location. *Opt Lett* **42**, 5141–5144 (2017).
79. Kryzhanovskaya NV, Zubov FI, Moiseev EI et al. On-chip light detection using integrated microdisk laser and photodetector bonded onto Si board. *Laser Phys Lett* **19**, 016201 (2022).
80. Kim G, Park H, Joo J et al. Single-chip photonic transceiver based on bulk-silicon, as a chip-level photonic I/O platform for optical interconnects. *Sci Rep* **5**, 11329 (2015).
81. Kacmoli S, Gmachl CF. Monolithic integration of quantum cascade lasers, detectors and active waveguides. In *CLEO: Science and Innovations 2022* STh5H. 4 (Optica Publishing Group, 2022). https://doi.org/10.1364/CLEO_SI.2022.STh5H.4.
82. Missinne J, Verplancke R, Chang YT et al. Microlenses on photonic integrated circuits enable flexible packaging and optical isolator integration. *Opt Laser Technol* **189**, 112940 (2025).
83. Jung E, Gehring H, Brückerhoff-Plückelmann F et al. Ultrabroadband plug-and-play photonic tensor core packaging with sub-dB loss. *Sci Adv* **11**, eadz1883 (2025).
84. Woon WY, Kasperovich A, Wen JR et al. Thermal management materials for 3D-stacked integrated circuits. *Nat Rev Electr Eng* **2**, 598–613 (2025).
85. Milanizadeh M, Aguiar D, Melloni A et al. Canceling thermal cross-talk effects in photonic integrated circuits. *J Lightwave Technol* **37**, 1325–1332 (2019).
86. Sun C, Wade MT, Lee Y et al. Single-chip microprocessor that communicates directly using light. *Nature* **528**, 534–538 (2015).
87. Shekhar S, Bogaerts W, Chrostowski L et al. Roadmapping the next generation of silicon photonics. *Nat Commun* **15**, 751 (2024).
88. Ranno L, Gupta P, Gradkowski K et al. Integrated photonics packaging: challenges and opportunities. *ACS Photonics* **9**, 3467–3485 (2022).
89. Das Sharma D, Pasdast G, Tiagaraj S et al. High-performance, power-efficient three-dimensional system-in-package designs with universal chiplet interconnect express. *Nat Electron* **7**, 244–254 (2024).
90. Trappen M, Blaicher M, Dietrich PI et al. 3D-printed optical probes for wafer-level testing of photonic integrated circuits. *Opt Express* **28**, 37996–38007 (2020).

91. Culemann D, Knuettel A, Voges E. Integrated optical sensor in glass for optical coherence tomography (OCT). *IEEE J Select Topics Quantum Electron* **6**, 730–734 (2000).
92. Margallo-Balbás E, Geljon M, Pandraud G et al. Miniature 10 kHz thermo-optic delay line in silicon. *Opt Lett* **35**, 4027–4029 (2010).
93. Choudhary OP, Chouksey S, Sen PK et al. MOEMS optical delay line for optical coherence tomography. *J Phys Conf Ser* **534**, 012066 (2014).
94. Yurtsever G, Dumon P, Bogaerts W et al. Integrated photonic circuit in silicon on insulator for Fourier domain optical coherence tomography. *Proc SPIE* **7554**, 75541B (2010).
95. Yurtsever G, Komorowska K, Baets R. Low dispersion integrated Michelson interferometer on silicon on insulator for optical coherence tomography. In *European Conference on Biomedical Optics 2011* 80910T (Optica Publishing Group, 2011). https://doi.org/10.1364/ECBO.2011.80910T.
96. Nguyen VD, Weiss N, Beeker W et al. Integrated-optics-based swept-source optical coherence tomography. *Opt Lett* **37**, 4820–4822 (2012).
97. Yurtsever G, Weiss N, Kalkman J et al. Ultra-compact silicon photonic integrated interferometer for swept-source optical coherence tomography. *Opt Lett* **39**, 5228–5231 (2014).
98. Huang YY, Badar M, Nitkowski A et al. Wide-field high-speed space-division multiplexing optical coherence tomography using an integrated photonic device. *Biomed Opt Express* **8**, 3856–3867 (2017).
99. Hainberger R, Muellner P, Nevlacsil S et al. Silicon-nitride waveguide-based integrated photonic circuits for medical diagnostic and other sensing applications. *Proc SPIE* **10922**, 1092204 (2019).
100. Van Leeuwen TG, Akca IB, Angelou N et al. On-chip Mach-Zehnder interferometer for OCT systems. *Adv Opt Technol* **7**, 103–106 (2018).
101. Akca BI, Nguyen VD, Kalkman J et al. Toward spectral-domain optical coherence tomography on a chip. *IEEE J Select Topics Quantum Electron* **18**, 1223–1233 (2012).
102. Nevlacsil S, Muellner P, Maese - Novo A et al. PECVD SiN photonic integrated circuit for swept source OCT at 840 nm. ECIO 2020, Pairs, June 23-24 2020.
103. Wang Z, Lee HC, Vermeulen D et al. Silicon photonic integrated circuit swept-source optical coherence tomography receiver with dual polarization, dual balanced, in-phase and quadrature detection. *Biomed Opt Express* **6**, 2562–2574 (2015).
104. Chang LT, Weiss N, van Leeuwen TG et al. Chip based common-path optical coherence tomography system with an on-chip microlens and multi-reference suppression algorithm. *Opt Express* **24**, 12635–12650 (2016).
105. Schneider S, Lauermann M, Dietrich PI et al. Optical coherence tomography system mass-producible on a silicon photonic chip. *Opt Express* **24**, 1573–1586 (2016).
106. Eggleston MS, Pardo F, Bolle C et al. 90dB sensitivity in a chip-scale swept-source optical coherence tomography system. In *CLEO: Applications and Technology 2018* JTh5C. 8 (Optica Publishing Group, 2018). https://doi.org/10.1364/CLEO_AT.2018.JTh5C.8.
107. Sancho-Durá J, Zinoviev K, Lloret-Soler J et al. Handheld multimodal imaging for point-of-care skin diagnosis based on akinetic integrated optics optical coherence tomography. *J Biophotonics* **11**, e201800193 (2018).
108. Chen SY, Potsaid B, Li Y et al. High speed, long range, deep penetration swept source OCT for structural and angiographic imaging of the anterior eye. *Sci Rep* **12**, 992 (2022).
109. Nguyen VD, Akca BI, Wörhoff K et al. Spectral domain optical coherence tomography imaging with an integrated optics spectrometer. *Opt Lett* **36**, 1293–1295 (2011).
110. Akca BI, Považay B, Chang L et al. Advanced integrated spectrometer designs for miniaturized optical coherence tomography systems. *Proc SPIE* **8802**, 880202 (2013).
111. Akca BI, Považay B, Alex A et al. Miniature spectrometer and beam splitter for an optical coherence tomography on a silicon chip. *Opt Express* **21**, 16648–16656 (2013).
112. Nitkowski A, Preston K, Sherwood-Droz N et al. On-chip spectrometer for low-cost optical coherence tomography. *Proc SPIE* **8934**, 89340F (2014).
113. Yurtsever G, Považay B, Alex A et al. Photonic integrated Mach-Zehnder interferometer with an on-chip reference arm for optical coherence tomography. *Biomed Opt Express* **5**, 1050–1061 (2014).
114. Ruis RM, Leinse A, Dekker R et al. Decreasing the size of a spectral domain optical coherence tomography system with cascaded arrayed waveguide gratings in a photonic integrated circuit. *IEEE J Select Topics Quantum Electron* **25**, 6100109 (2019).
115. Seyringer D, Sagmeister M, Maese-Novo A et al. Compact and high-resolution 256-channel silicon nitride based AWG-spectrometer for OCT on a chip. In *2019 21st International Conference on Transparent Optical Networks (ICTON)* 1–4 (IEEE, 2019). https://doi.org/10.1109/ICTON.2019.8840473.
116. Seyringer D, Sagmeister M, Maese-Novo A et al. Technological verification of size-optimized 160-channel silicon nitride-based AWG-spectrometer for medical applications. *Appl Phys B* **125**, 88 (2019).
117. Zheng HY, Chen BL, Lu HY et al. Bidirectional coupler study for chip-based spectral-domain optical coherence tomography. *Micromachines* **13**, 373 (2022).
118. Zhang ZY, Wang Y, Wang JR et al. Integrated scanning spectrometer with a tunable micro-ring resonator and an arrayed waveguide grating. *Photon Res* **10**, A74–A81 (2022).
119. Agneter A, Muellner P, Nguyen Q et al. CMOS optoelectronic spectrometer based on photonic integrated circuit for in vivo 3D optical coherence tomography. *PhotoniX* **5**, 31 (2024).
120. Ji XC, Yao XW, Gan Y et al. On-chip tunable photonic delay line. *APL Photon* **4**, 090803 (2019).
121. Sharma B, Kishor K, Sharma S et al. Design and simulation of broadband beam splitter on a silicon nitride platform for optical coherence tomography. *Fiber Integr Opt* **38**, 247–257 (2019).
122. Widhianto BYB, Lu YT, Chang WC et al. Broadband coupler manipulation through particle swarm optimization for arrayed waveguide grating based optical coherence tomography. *IEEE Photon J* **13**, 6600613 (2021).
123. Dong Y, Yang JY, Xu Y et al. On-chip beam splitting strategies based on SWG assisted directional coupler for 850 nm optical coherence tomography-a numerical study. *IEEE Photon J* **13**, 6600312 (2021).
124. Tsai TH, Fujimoto JG, Mashimo H. Endoscopic optical coherence tomography for clinical gastroenterology. *Diagnostics* **4**, 57–93 (2014).
125. Everett M, Magazzeni S, Schmoll T et al. Optical coherence tomography: from technology to applications in ophthalmology. *Transl Biophotonics* **3**, e202000012 (2021).
126. Yabushita H, Bouma BE, Houser SL et al. Characterization of human atherosclerosis by optical coherence tomography. *Circulation* **106**, 1640–1645 (2002).
127. Muijzer MB, Schellekens PAWJ, Beckers HJM et al. Clinical applications for intraoperative optical coherence tomography: a systematic review. *Eye* **36**, 379–391 (2022).
128. Krebs I, Binder S, Stolba U et al. Optical coherence tomography guided retreatment of photodynamic therapy. *Br J Ophthalmol* **89**, 1184–1187 (2005).
129. Salinas-Alamán A, García-Layana A, Maldonado MJ et al. Using optical coherence tomography to monitor photodynamic therapy in age related macular degeneration. *Am J Ophthalmol* **140**, 23.e1–23.e7 (2005).

130. García-Layana A, Salinas-Alamán A, Maldonado MJ et al. Optical coherence tomography to monitor photodynamic therapy in pathological myopia. *Br J Ophthalmol* **90**, 555–558 (2006).
131. Sirotkina MA, Matveev LA, Shirmanova MV et al. Photodynamic therapy monitoring with optical coherence angiography. *Sci Rep* **7**, 41506 (2017).
132. Sirotkina MA, Moiseev AA, Matveev LA et al. Accurate early prediction of tumour response to PDT using optical coherence angiography. *Sci Rep* **9**, 6492 (2019).
133. Gubarkova EV, Feldchtein FI, Zagaynova EV et al. Optical coherence angiography for pre-treatment assessment and treatment monitoring following photodynamic therapy: a basal cell carcinoma patient study. *Sci Rep* **9**, 18670 (2019).
134. Hamdoon Z, Jerjes W, Rashed D et al. In vivo optical coherence tomography-guided photodynamic therapy for skin pre-cancer and cancer. *Photodiagn Photodyn Ther* **36**, 102520 (2021).
135. Nie HH, Wang F, Xiong QZ et al. Novel biliopancreatic duct endoscope combining optical coherence tomography with intraductal US for exploring the bile duct: a diagnostic study in a porcine model. *Gastrointest Endosc* **94**, 1136–1142 (2021).
136. Pahlevaninezhad H, Lee AMD, Marsh R et al. An endoscopic imaging system for co-registered Doppler optical coherence tomography and autofluorescence imaging of human airways *in vivo*. In *Bio-Optics: Design and Application 2015* BM4A. 4 (Optica Publishing Group, 2015). https://doi.org/10.1364/BODA.2015.BM4A.4.
137. Zhang HH, Yang B, Li SQ et al. Retinal OCT image segmentation with deep learning: a review of advances, datasets, and evaluation metrics. *Comput Med Imag Grap* **123**, 102539 (2025).
138. Ma YH, Chen XJ, Zhu WF et al. Speckle noise reduction in optical coherence tomography images based on edge-sensitive cGAN. *Biomed Opt Express* **9**, 5129–5146 (2018).
139. Miladinović A, Biscontin A, Ajčević M et al. Evaluating deep learning models for classifying OCT images with limited data and noisy labels. *Sci Rep* **14**, 30321 (2024).
140. Devalla SK, Subramanian G, Pham TH et al. A deep learning approach to denoise optical coherence tomography images of the optic nerve head. *Sci Rep* **9**, 14454 (2019).
141. Lee W, Nam HS, Seok JY et al. Deep learning-based image enhancement in optical coherence tomography by exploiting interference fringe. *Commun Biol* **6**, 464 (2023).
142. Seong D, Han S, Kang DW et al. Development of single-board computer-based temperature-insensitive compact optical coherence tomography for versatile applications. *IEEE Trans Instrum Meas* **73**, 4504609 (2024).
143. Zhang Z, Huang BJ, Zhang ZY et al. On-chip reconstructive spectrometer based on parallel cascaded micro-ring resonators. *Appl Sci* **14**, 4886 (2024).
144. You CY, Li X, Hu YH et al. CMOS compatible reconstructive spectrometers with self-referencing integrated Fabry-Perot resonators. *Proc Natl Acad Sci USA* **121**, e2403950121 (2024).
145. Liao K, Lian YX, Yu MT et al. Hetero-integrated perovskite/Si_3N_4 on-chip photonic system. *Nat Photon* **19**, 358–368 (2025).

Acknowledgements

This work was financially supported by the National Natural Science Foundation of China under Grant (62205306); Fudan University through the Research Initiation Project (IDH2323007Y, IDH2323008Y, IDH2323010Y) and the National Natural Science Foundation of China.

Q. Q. Song thanks the financial support from the National Natural Science Foundation of China under Grant (62205306). G. Li thanks the financial support from Fudan University through the Research Initiation Project (IDH2323007Y, IDH2323008Y， IDH2323010Y) and the National Natural Science Foundation of China.

Author contributions

Writing-original draft preparation: Q. Q. S. Writing-review and editing: Q.Q. S, G. Q. L. Review, editing and discussion: D. Z, Q. Q. S, G. Q. L, Z. D. All authors read and approved the final manuscript.

Competing interests

The authors declare no competing financial interests.